Science
AAAS

Supplementary Materials for

A viral RNA hijacks host machinery using dynamic conformational changes of a tRNA-like structure

Steve L. Bonilla *et al.*

Corresponding author: Jeffrey S. Kieft, jeffrey.kieft@cuanschutz.edu

Science **374**, 955 (2021)
DOI: 10.1126/science.abe8526

The PDF file includes:

Other Supplementary Material for this manuscript includes the following:

MATERIALS AND METHODS

In vitro transcription, purification, and folding of RNA

Templates for *in vitro* transcription were generated by PCR amplification of sequence-verified double-stranded DNA fragments (gBlocks; Integrated DNA Technologies). Sequences for all constructs are provided in Table S2. To reduce the amount of N+1 products generated by *in vitro* transcription and ensure correct termination at CCA_{OH}, which is necessary for aminoacylation, PCR amplification was performed using a reverse primer with a 2′OMe modification at the second 5′ nucleotide, as described previously (*36*).

The gBlocks were synthesized with a 'GG' added at the 5' end of the sequences of interest to facilitate transcription by T7 RNA polymerase. The transcription reactions contained 8 mM of each NTP (ATP, UTP, CTP, and GTP), 60 mM $MgCl_2$, 30 mM Tris, pH 8.0, 10 mM DTT, 0.1% spermidine, 0.1% Triton X-100, 0.24 U/µl RNasin RNase inhibitor (Promega), and ~ 0.14 mg/ml T7 RNA polymerase (in-house prepared). The transcription reactions were incubated for 3 hrs at 37°C. For constructs with 5′ and/or 3′ self-excising ribozymes (Table S2), the concentration of $MgCl_2$ was increased to 120 mM after the 3 hrs transcription reaction and the constructs were incubated for an additional 15 minutes at 60°C. The transcribed RNA constructs were ethanol precipitated, purified by denaturing gel electrophoresis (8% polyacrylamide), cleaned using AMPure XP magnetic beads (Beckman Coulter), and buffer exchanged into RNase free water using 10 kD cutoff Amicon centrifugal filters (Millipore).

As one of the negative controls for BMV TLS aminoacylation, we produced BMV TLS (2'–3' cP), which is identical to BMV TLS except for a terminal 2′-3′ cyclic phosphate that prevents efficient aminoacylation. To introduce the terminal 2′-3′ cyclic phosphate, a 69 nt hepatitis delta virus (HDV) self-excising ribozyme was introduced 3′ of the wild type BMV TLS sequence. BMV TLS (2'–3' cP) was transcribed, cleaved, and purified using the protocol described above. The product of the ribozyme cleavage results in the production of the terminal 2′-3′ cyclic phosphate.

To fold the RNAs into their native conformation, the RNAs were resuspended at the desired concentration into a buffer solution containing 50 mM MOPS pH 7.0, 30 mM Na^+, and 10 mM $MgCl_2$, incubated at 80-90°C for 1 minute and cooled down to 23°C for 15 minutes.

Preparation of TyrRS for aminoacylation assays and cryo-EM studies

To test the aminoacylation capacity of our BMV TLS RNA constructs and for cryo-EM studies of TyrRS and of the BMV TLS-TyrRS complex, we used TyrRS from a model host of BMV, *Phaseolus vulgaris* (common bean), as previous studies have shown that this variant efficiently tyrosylates BMV RNA *in vitro* (*39*). We obtained the sequence of this TyrRS from the UniProt database (gene: PHAVU_002G027700g) and optimized it for expression in *E. coli* using the online Integrated DNA Technologies (IDT) Codon Optimization Tool. A gBlock encoding the TyrRS sequence, cleavage sequences for restriction enzymes NdeI and BamHI, and a 6-His-tag was cloned into a pET15b vector using standard molecular biology techniques for ligation with T4 DNA ligase. The protein was expressed in BL21 (DE3) cells in Luria broth (LB) containing ampicillin at 37°C until OD600 reached 0.6 and then protein production was induced with the addition of 0.5 mM IPTG for 4 hours. The cells were harvested by centrifugation at 5488 x g for 12 minutes at 6°C. The pellets were resuspended in lysis buffer (20 mM Tris-HCl pH 7.0, 500 mM NaCl, 2 mM β-mercaptoethanol, 10% glycerol, and 1 EDTA-free protease inhibitor tab (Roche)) and sonicated for a total of 2 minutes (20 sec on and 40 sec off intervals) at 75% amplitude. The lysate was centrifuged at 30,000 x g for 30 min at 4°C before being loaded into a gravity flow column (Bio-Rad) and purified by Ni-NTA resin (UBP Bio) followed by size exclusion using FPLC and a Sepax 300 SEC column. The TyrRS protein was stored at a concentration of 10 μM (based on MW of dimer) in buffer containing 20 mM Tris-HCl pH 7.5, 150 mM NaCl, 2 mM β-mercaptoethanol, and 10% glycerol.

Aminoacylation assays

Aminoacylation of sample used for cryo-EM studies. Tyrosylation of BMV TLS and control RNAs was assayed using a protocol adapted from a previous study of TYMV TLS^{Val} (*36*). Briefly, the RNAs were

folded by heating and cooling in a buffer containing 10 mM $MgCl_2$, 30 mM Na^+, and 50 mM MOPS pH 7.0, as described above. The RNAs were diluted to 10 X the final reaction concentrations (0 – 100 nM; Fig. 1B). Prior to the aminoacylation experiment, the TyrRS was exchanged into a buffer containing 50 mM Tris pH 8.0, 5 mM $MgCl_2$, 1 mM TCEP, and 5% glycerol using an Amicon 30 kD cutoff centrifugal filter and diluted to 1 μM (based on the MW of the dimer). The reaction buffer consisted of 2 mM ATP, 30 mM KCl, 5 mM $MgCl_2$, 5 mM DTT, and 30 mM HEPES-KOH pH 8.0. The total volume of each aminoacylation reaction was 20 μl. Reaction buffer, TyrRS solution (final concentration of TyrRS was 100 nM), and folded RNA solution (final concentration of RNA was 0 – 100 nM) were mixed and incubated on ice. The aminoacylation reaction was initiated by the addition of 1 μl of ^{3}H-labeled L-tyrosine (40 – 60 Ci/mmol) and followed by incubation at 30^{o}C for 30 min. The reactions were then diluted by adding 200 μl of wash buffer (20 mM Bis-tris pH 6.5, 10 mM NaCl, 1 mM $MgCl_2$, and trace amounts of bromophenol blue dye) and immediately filtered by depositing the diluted reaction solution into a well of a Minifold I 96 well dot-blot system (Whatman). Using the dot-blot system, the reaction solution was filtered through a layer of Tuffryn membrane (PALL Life Sciences), Hybond positively charged membrane (GE Healthcare), and gel dryer filter paper (Bio-Rad). The negatively charged RNA binds to the Hybond membrane. Immediately after the diluted reaction solution ran through the filter membranes, 600 μl of wash buffer was added to the well and allowed to flow through the membranes. The Hybond membrane was allowed to dry, and the locations marked by the bromophenol blue from the wash buffer were cut out. A scintillation counter (Perkin-Elmer Tri-Carb 2910 TR) was used to measure the radioactivity of the Hybond membrane pieces.

Comparison of BMV TLS UUCG mutants. Wild type BMV TLS and mutants with UUCG at the apical loops of B3, B2, or E (Table S4) were transcribed and purified as described above. The RNAs were folded in 10 mM $MgCl_2$, 30 mM Na^+, and 50 mM MOPS pH 7.0 at a concentration of 1.2 μM. Three microliters of TyrRS stock solution ([TyrRS dimer] = 10 μM in 20 mM Tris-HCl pH 7.5, 150 mM NaCl, 2 mM β-mercaptoethanol, and 10% glycerol) was added to 27 μl of buffer containing 50 mM Tris pH 8.0, 5 mM $MgCl_2$, 1 mM TCEP, and 5% glycerol. A 10X reaction buffer consisted of 20 mM ATP, 300 mM KCl, 50

mM $MgCl_2$, 50 mM DTT, and 300 mM HEPES-KOH pH 8.0. The total volume of each aminoacylation reaction was 20 µl. For each reaction we added 13 µl of water, 2 µl of 10X reaction buffer, 2 µl of 1.2 µM RNA, 2 µl of 1 µM TyrRS dimer solution, and 1 µl of ^{3}H-labeled L-tyrosine (40 – 60 Ci/mmol). The final concentrations of RNA and TyrRS dimer in the reaction were 120 and 100 nM, respectively. The reactions were incubated for 5 minutes at 30ºC. After this time, 80 µl of wash buffer (20 mM Bis-tris pH 6.5, 10 mM NaCl, 1 mM $MgCl_2$, and trace amounts of bromophenol blue dye) were added to the reaction, mixed, and quickly filtered through the blotting apparatus described above. An additional 500 µl of washing buffer were flown through the filter. The Hybond membrane was allowed to dry overnight, and the locations marked by the bromophenol blue were cut out. Radioactivity of the Hybond membrane was measured with a scintillation counter as described above.

Bioinformatic analysis of TLS^{Tyr} variants

To build a sequence and secondary structure consensus model of TLS^{Tyr}, we used a preliminary alignment of the TLS^{Tyr} class obtained from the Rfam database (family RF01084) as a starting point, which contained eight sequences lacking the 5′ end of the structure corresponding to stems E and B3 stems (*37, 38*). These eight sequences were manually expanded to include the additional base pairing elements based on published secondary structure models for BMV TLS. Homology searches were performed using Infernal (*40*) to query a database of positive sense RNA viral sequences, resulting in 512 unique sequences derived from eleven distinct viruses, all in the *Bromoviridae* family (Data S1). We evaluated the resulting alignment for nucleotide sequence conservation, as well as significant covariation of base pairing elements, using RNA Structural Covariation Above Phylogenetic Expectation (R-scape) (*41*) analysis to generate a consensus sequence and secondary structure model of TLS^{Tyr} RNAs.

SHAPE chemical probing

A published protocol was used to probe the secondary structure of representative TLS^{Tyr} variants using *N*-methyl isatoic anhydride (NMIA) as a chemical modifier (*42*). Briefly, the RNAs were folded to

their native conformations using the steps described above and reacted for 30 minutes at 23°C with either NMIA or DMSO (control). The reactions contained 3 mg/ml NMIA or DMSO, 50 mM HEPES-KOH pH 8.0, 10 mM $MgCl_2$, 60 mM RNA, and 3 nM fluorescently labeled DNA primer for reverse transcription. The reactions were then quenched by adding NaCl to a final concentration of 500 mM and Na-MES pH 6.0 to final concentration of 50 mM. Magnetic beads with poly-dT strands complementary to a poly-A sequence contained within the DNA primer were used to purify the RNA using a magnetic stand (Invitrogen Poly(A)Purist MAG Kit). After purification, the RNAs were resuspended in water to ~ 240 nM. The RNAs were then reverse transcribed using SuperScript III (Invitrogen) by incubating at 50°C for 45 minutes and degraded by the addition of NaOH to a final concentration of 200 mM followed by incubation for 5 minutes at 90°C. The reactions were quenched by addition of an acidic solution (final concentrations: 250 mM sodium acetate pH 5.2, 250 mM HCl, 500 mM NaCl). To produce RNA ladders, separate reverse transcriptions were performed with each of four ddNTPs (TriLink BioTechnologies). The remaining DNA was then purified using the magnetic stand and eluted in a solution containing HiDi formamide (ThermoFisher) and trace amounts of GeneScan 500 ROX Dye Size Standard (ThermoFisher). Capillary electrophoresis (Applied Biosystems 3500 XL) was used to probe the remaining fluorescently labeled DNA products. Data analysis, including background subtraction and signal normalization using the reactivity of flanking hairpins common to all constructs, was performed using the HiTrace RiboKit computational toolkit (https://ribokit.github.io/HiTRACE/), as described previously (*43-45*).

Cryo-EM grid preparation and imaging

Imaging of BMV TLS RNA. Cryo-EM grids with RNA samples were prepared using a standard procedure. Briefly, C-Flat holey carbon grids (hole size: 1.2 µm; spacing: 1.3 µm; mesh: 400; Electron Microscopy Sciences) were cleaned with a Gatan Solarus Model 950 advanced plasma system. The settings of the plasma cleaner were 'Cleaning time' : 6 seconds, 'Vacuum target': 70 mTorr, 'Vacuum range': 0 mTorr, 'Pumping switch point': 20 Torr, 'Turbo pump speed': 750 Hz, 'O_2 gas flow': 27.5 sccm, 'H_2 gas flow': 6.4 sccm, 'Air gas flow': 0.0 sccm, 'Gas flow timeout': 20 seconds, 'Forward RF target': 50 W, 'Forward

RF range': 5 W, 'Maximum reflected RF': 5 W, 'RF tuning timeout': 4 seconds, 'RF tunning attempts': 3. Then, 3 µl of folded RNA solution (final concentrations: 10 – 25 µM RNA, 10 mM $MgCl_2$, 30 mM Na^+, 50 mM MOPS pH 7.0) was deposited on each grid and a FEI Vitrobot Mark IV was used to plunge freeze the grids using liquid ethane. The temperature of the Vitrobot chamber was set to 4°C and the humidity to 100%. Blot time was set to 2.5 seconds, wait time to 0 seconds, and blot force to –5. Filter paper was used for blotting (Prod No. 47000-100, Ted Pella, INC.). Grid screening and generation of low to moderate resolution maps were performed using a ThermoFisher Talos Arctica transmission electron microscope (TEM) operating at an accelerating voltage of 200 kV and equipped with a Gatan K3 Summit direct electron detector (DED). Leginon software was used to collect data on this microscope. For wild type BMV TLS RNA, we collected 2389 movies (50 frames) at a magnification of 45,000 (raw pixel size: 0.899 Å) with defocus ranging from –1 to –2.5 µm. The total dose was ~60 electrons/$Å^2$. For the $B3^{ext}$+C^{short} construct we collected 2494 movies (60 frames) with a total dose of ~75 electrons/$Å^2$ and for the D^{ext}+$B2^{short}$ construct we collected 505 movies (60 frames) with a total dose of ~75 electrons/$Å^2$. Magnification and defocus range were the same for all three constructs: wild type BMV TLS, $B3^{ext}$+C^{short}, and D^{ext}+$B2^{short}$. To obtain a higher-resolution map of BMV TLS RNA we used a ThermoFisher Krios TEM equipped with a Falcon 3 DED and a Bioquantum K3 imaging filter at the Pacific Northwest Cryo-EM Center (PNCC). Data was collected in super resolution mode with a pixel size of 0.413 Å. SerialEM software was used to collect data on this microscope. We collected 9746movies (28 frames) with a total dose of 30 electrons/$Å^2$ and a defocus range of –0.8 to –2.0 µm (Table S1).

Imaging BMV TLS-TyrRS complex. Folded BMV TLS RNA was mixed with purified TyrRS and incubated for 5 minutes at room temperature, then the sample was placed in ice prior to being deposited on plasma-cleaned C-Flat holey carbon grids (hole size: 1.2 µm; spacing: 1.3 µm; mesh: 400; Electron Microscopy Sciences) and plunge freezing with the Vitrobot. The settings of the plasma cleaner and the Vitrobot were the same as for BMV TLS RNA described above. The final solution contained ~5 uM TyrRS dimer, ~10 uM BMV TLS RNA, 5 mM $MgCl_2$, 75 mM NaCl, 25 mM MOPS (with 15 mM Na^+ from NaOH titration),

10 mM Tris-HCl, 1 mM β-mercaptoethanol, and 5% glycerol. Preliminary data was collected with the 200 kV Talos Arctica TEM using the same settings as those described above for BMV TLS RNA. Higher-resolution data was collected at PNCC with the 300 kV ThermoFisher Krios. The data was collected in super resolution mode with a pixel size of 0.415 Å. SerialEM software was used for the data collection. To reduce the effect of preferred orientations, data was collected at different tilt angles. In total we collected 4302 movies at 0°, 4158 at 20°, and 2502 at 45°. Data at 0° and at 20° were collected from the same grid and data at 45° was collected on a different grid. Movies contained 60 frames and were collected using a total dose of 60 electrons/Å^2, and a defocus range of –0.8 to –2.5 μm (Table S1).

Imaging of isolated TyrRS homodimer. Three microliters of TyrRS solution containing 10 mM TyrRS dimer, 20 mM Tris-HCl pH 7.5, 150 mM NaCl, 2 mM β-mercaptoethanol, and 10% glycerol was deposited on plasma-cleaned C-Flat holey carbon grids (hole size: 1.2 μm; spacing: 1.3 μm; mesh: 400; Electron Microscopy Sciences) before plunge freezing with Vitrobot. The settings of the plasma cleaner and the Vitrobot were the same as those used for BMV TLS RNA described above. A dataset of 961 movies (60 frames) was collected with our 200 kV Arctica using the same settings as described above for BMV TLS RNA.

Cryo-EM data analysis

General protocol for all samples. Cryo-EM data was processed using cryoSPARC (*17*). The protocols used for each sample are summarized in Fig. S2-S3 for BMV TLS RNAs, Fig. S11 for the BMV TLS-TyrRS complex, and Fig. S13 for the isolated TyrRS enzyme. For all datasets, movies were imported into cryoSPARC, and motion correction ('Patch motion correction' in cryoSPARC) and CTF estimation ('Patch CTF estimation' in cryoSPARC) were performed using default parameters. Exposures were curated to eliminate those with obvious defects such as damaged grid areas or excessive ice contamination. Several different methods of picking particles were used, all of which produced essentially identical 3D maps after classification and removal of junk particles, with only small differences in the final resolution of the maps.

These methods included manual particle-picking (typically picked > 3000 particles), automated 'blob picker' in cryoSPARC, and using low pass filtered templates generated from atomic models. The initial particles picked (by one of the methods described above) were 2D classified to generate templates for automated picking. We also tested Relion (*46*) for the task of generating 2D templates for particle picking, but the quality of the 2D classes was worse than with cryoSPARC. Automatically picked particles were 2D classified to remove 'junk' and used for *ab initio* 3D reconstructions using stochastic gradient descent implemented in cryoSPARC (*17*). In some cases, *ab initio* reconstructions were performed without prior 2D classification of the particles, and junk was removed afterwards using 3D classification. These two methods essentially produced the same results, with only minor differences in the final resolution of the maps. 3D classification (heterogenous refinement in cryoSPARC), homogeneous, and non-uniform refinements were performed to produce final maps. Resolution was estimated using gold standard Fourier shell correlation (GSFSC) of 0.143. The resolution reported was corrected for high-resolution noise by the cryoSPARC refinement algorithms.

Generating 3D maps of BMV TLS RNAs. For BMV TLS RNA with the 200 kV TEM, we manually picked ~ 3000 particles and classified them to generate templates for automated particle picking (Fig. S2). The putative particles (n = 729, 843) were extracted with a box size of 340 pixels (pixel size: 0.899 Å) and subjected to several rounds of 2D classification to remove junk. The remaining particles (n = 422,021) were used in several *ab initio* 3D reconstructions, varying in the numbers of required classes (Fig. S2). The reconstructions consistently generated a volume with clear RNA secondary structure features (i.e., A-form helices and grooves) and a size consistent with BMV TLS RNA, and other volumes that resembled the main volume but were less defined (Fig. S2). Later atomic modelling of the secondary structure of BMV TLS into the well-defined volume as well as cryo-EM data of BMV TLS RNA bound to TyrRS confirmed that this volume corresponded to the correct folded functional conformation of BMV TLS. To remove potential remaining junk, we generated three *ab initio* volumes and selected the particles that grouped with the well-

defined BMV TLS volume (n = 185,596). These particles were used to refine the volume to 7.01 Å resolution (Fig. S2).

For BMV TLS RNA with the 300 kV TEM (Fig. S3), we used blob picker on a subset of 500 micrographs and subjected the blobs to 2D classification to generate templates for automated picking in all 9,746 micrographs (Fig. S3). All picked particles were extracted with a 600 pixels box (pixel size = 0.415 Å) and were used to produce three *ab initio* volumes (Fig. S3). The results were consistent with the 200 kV data, reproducing the well-defined volume with RNA secondary structure features and other volumes that were not well defined and were presumably built partly from junk. To remove junk particles, the 'bad' volumes were used as particle 'sinks' in multiple rounds of 3D classification ('Heterogenous refinement' in cryoSPARC) (Fig. S3). The global features of the well-defined BMV TLS RNA volume remained unchanged during each round of 3D classification but the resolution was incrementally better. The particles remaining after several rounds of 3D classification (n = 128,266) were used in homogenous and non-uniform refinements to generate a final map with a resolution of 4.3 Å. Maps for the engineered BMV TLS constructs with extensions and truncations were generated using this same protocol. Stem B3 in modified construct $B3^{ext}+C^{short}$, which was 5 bp longer than the original stem, displayed great flexibility and was difficult to visualize in the refined map. To better visualize this stem, we performed a '3D Variability Analysis' in cryoSPARC (*17*) to divide a map into an ensemble and this analysis better revealed the extended B3. In this analysis, the number of modes to solve was set to 3, symmetry to C1 (default), filter resolution to 10 Å, filter order to 1.5 (default), high pass order to 1.5 (default), number of iterations to 20 (default), and Lamda to 0.01 (default). The results from the 3D variability analysis were imported into a '3D variability display' with the output mode set to 'simple' and the number of frames set to 20. The first mode was imported into Chimera and displayed as a series of 20 volumes, some of which more clearly showed the position of the extended B3. Importantly, none of the other helices (except for the shortened C) displayed noticeable differences relative to wild type BMV TLS. The volume with the best defined B3 was used to fit a structural model (Fig. S7). A similar analysis was performed with wild type BMV TLS to generate Fig. 1F, with filter resolution set to 7.5 and number of frames set to 4 (as shown in Fig. 1F). The

four volumes generated from this analysis were then used to reclassify the particles and each volume was refined separately using 'homogeneous refinement' in cryoSPARC.

Generating 3D maps of TLS-TyrRS complex. For the complex, we started our analysis with micrographs collected without tilt (n = 4302). To generate initial 2D templates, we picked particles on a subset of 126 micrographs using 'blob picker' in cryoSPARC with particle size range set to 70–200 Å (Fig. S11A). The templates were used for automated particle picking in the 4302 micrographs. After removal of junk particles using 2D classification, 374,993 particles were used to generate *ab initio* 3D reconstructions that clearly showed density consistent with BMV TLS RNA bound to TyrRS (Fig. S11A). Only one bound RNA appeared well defined in the reconstructions, as explained in Results and Discussion. A model generated from these initial reconstructions was used to simulate 2D templates for picking particles in all the micrographs, including those with 0°, 20°, and 45° tilts (Fig. S11B). We then performed several rounds of 2D classification to remove junk particles and combined the particles from all tilts, resulting in 783,472 particles that were used for the *ab initio* reconstruction of four maps (Fig. S11B). The maps clearly showed BMV TLS RNA bound to TyrRS in two distinct conformations. Several rounds of 3D classification followed by homogeneous and non-uniform refinements generated maps with 5.5 and 6.0 Å resolution maps for each of the two conformations (Fig. S12).

Generating 3D map of isolated TyrRS dimer. We used the crystal structure of yeast TyrRS (PDB ID: 2DLC) to simulate a low-resolution (10 Å) EM map using Chimera (*47*) and produce 2D templates for particle picking. The particles were extracted with a 300 pixels box (pixel size: 0.899 Å). After one round of 2D classification to remove junk, we separated 2D projections that corresponded to the 'long' dimensions of TyrRS from those that corresponded to the 'short' dimensions, as done previously for an elongated protein of similar dimensions (*48*). Particles in the 'short' classes (n = 708,269) were subjected to a second round of classification using a circular mask of 120 Å and 'bad' classes (e.g., displaying more than one particle) were discarded. After discarding bad classes, 386,859 particles were used for *ab initio* reconstruction of

three models, one of which showed dimensions consistent with TyrRS (Fig. S13). This map was refined to 9.19 Å resolution using non-uniform refinement in cryoSPARC.

Structural modeling

Modeling of unbound BMV TLS RNA using molecular dynamics flexible fitting and real-space refinements and autoDRRAFTER. A schematic of the methods used to build the BMV TLS RNA structure is provided in Fig. S6. We began with the helical assignments obtained from the helical extensions/truncations and the published computational model of the BMV TLS RNA (*19*), which agreed well with the known secondary structure. Each helical domain was extracted from the published model and docked into the corresponding density using UCSF Chimera (*47*). Manual modeling was performed in Chimera and interactive automated modelling in Coot (*49*) to join the helical domains and to obtain an initial model for flexible fitting (Fig S6A). We then performed molecular dynamics flexible fitting using the web server Namdinator (https://namdinator.au.dk/namdinator/) (*50*), with the following parameters: Map resolution: 4.3 Å, Start temperature: 298 K, Final temperature: 298 K, G-force Scaling Factor: 0.2, Minimization steps: 4000, Simulation steps: 20,000, Phenix RSR cycles: 1, Implicit solvent (GBIS): exclude. The resulting model was imported into Phenix (*51*) along with the cryo-EM map to perform additional real-space refinements (RSR), maintaining the secondary structure of the model during refinements. 'Minimization_global', 'local_grid_search' and 'adp' were selected in Phenix RSR, with Max Interations: 50, Macro cycles: 1, Target bonds rmsd: 0.0005, and Target angles rmsd: 1.5. Then the model and the cryo-EM map were imported into ERRASER to correct the RNA geometry (*52, 53*). Default settings were used in ERRASER. Several iterative rounds of PHENIX RSR and ERRASER were used to incrementally decrease steric clashes and improve the geometry of the model. Finally, we used 'Geometry minimization' under Model Tools in Phenix. The model validation statistics of the BMV TLS are listed in Table S1. These statistics were obtained using Phenix 'Comprehensive Validation (cryo-EM)' and the MolProbity web server (http://molprobity.biochem.duke.edu) (*54*). The outlier conformations were examined and were generally

located in complex areas of the structure expected to have non-canonical conformations. The same method was used to build structural models for engineered constructs $B3^{ext}$+C^{short} and D^{ext}+$B2^{short}$ (Fig. S7).

As an orthogonal method for modelling the structure of BMV TLS RNA we used autoDRRAFTER to generate ten models (*22*) (Fig. S6B). To do this we followed the steps described in the Rosetta Commons website (https://new.rosettacommons.org/docs/latest/application_documentation/rna/auto-drrafter#running-auto-drrafter) with the following parameters: convergence_threshold 10, nmodels 1000, njobs 10. The RMSD between the manually built structure and the autoDRRAFTER models were obtained using the 'align' command in Pymol (Schrödinger, Inc).

The structure of BMV TLS RNA was deposited in the Protein Data Bank under ID 7SAM and the cryo-EM maps in the Electron Microscopy Data Bank under ID EMD-24952.

Modelling of BMV TLS-TyrRS complex. We used the artificial intelligence protein prediction tool AlphaFold (*55*) incorporated into UCSF ChimeraX software (*56*) to predict the structure of the *Phaseolus vulgaris* TyrRS monomer. We also generated homology-based models using Modeller (*57*) and the I-Tasser web server (*58*) that agreed very well with the Alphafold prediction; the AlphaFold model displayed better geometry and molprobity statistics and therefore we used it for our final modelling of the TLS-TyrRS complex. To generate a model of 'bound state 1', two copies of the TyrRS monomer and the structure of unbound BMV TLS RNA were imported into Chimera and docked into the cryo-EM map. Domain B3+E was rotated manually to fit the density. The structure was then imported into Phenix to perform a real space refinement with options 'minimization_global', 'local_grid_search', and 'adp' selected. In the Phenix refinement, 'Macro cycles' was set to 1, 'Max iterations' to 100, 'Target bonds rmsd' to 0.01, and 'Target angles rmsd' to 1.0. Secondary structure and Ramachandran restraints were used during refinement. Model validation statistics for this structure are given in Table S1. The same process was used to generate a structure of 'bound state 2', with two macro cycles during real space refinement. The structures were deposited in the Protein Data Bank under IDs 7SC6 and 7SCQ for bound states 1 and 2, respectively. The

cryo-EM maps and half maps were deposited in the Electron Microscopy Data Bank under IDs EMD-25023 and EMD-25041 for bound states 1 and 2, respectively.

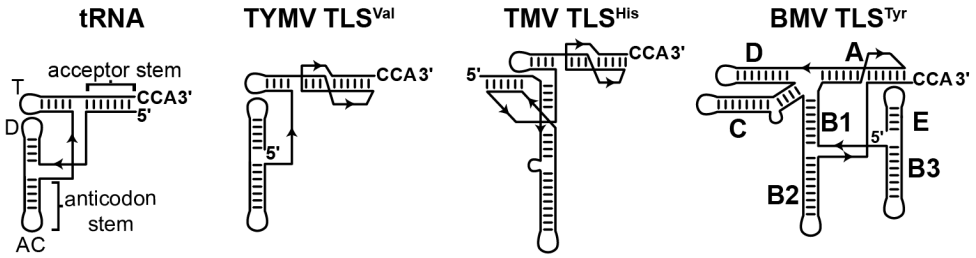

Fig. S1. Comparison of the secondary structures of tRNA and TLS from different classes. TLSs are classified based on their aminoacylation specificities. Three classes have been identified in viruses that infect plants: valylatable (TLS^{Val}), histidylatable (TLS^{His}), and tyrosylatable (TLS^{Tyr}) (*10*). Representatives from each class are shown. These are turnip yellow mosaic virus (TYMV), tobacco mosaic virus (TMV), and brome mosaic virus (BMV). The canonical structural features of tRNA are labeled: the anticodon and acceptor stems and the T, D and anticodon (AC) loops. The helical stems of BMV TLS are labeled with the names assigned in previous studies (*19*).

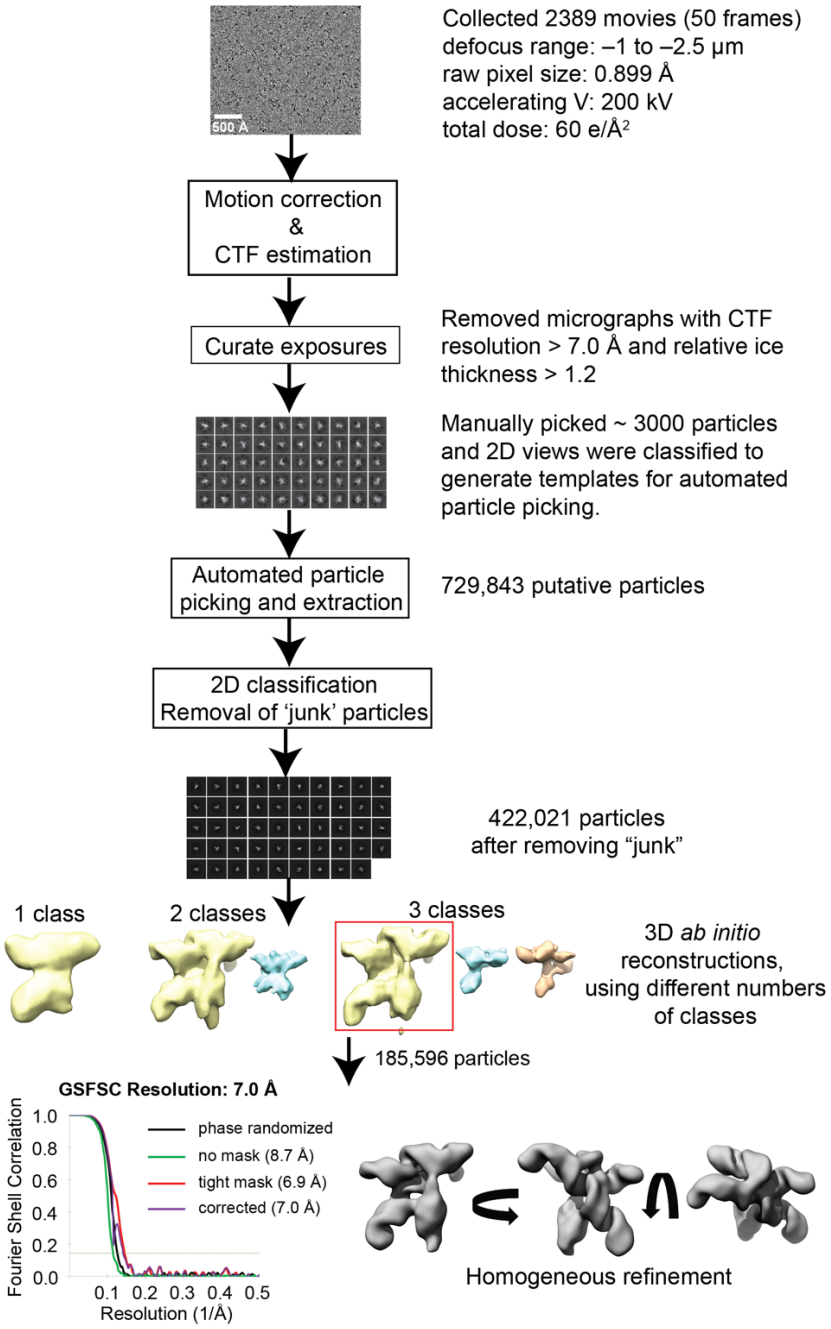

Fig. S2. Analysis of BMV TLS RNA data collected with 200 kV electron microscope. Steps followed to generate cryo-EM reconstruction of BMV TLS using cryoSPARC (*17*). *Ab initio* reconstructions were performed using different numbers of possible models. In every case, there was a reconstruction that was consistent with the size and expected topology of BMV TLS and that had clear RNA secondary structural features (yellow volumes). Cryo-EM experiments in the presence of TyrRS (see main text) confirmed that these maps corresponded to the functional conformation of BMV TLS. The BMV TLS map created with three classes was selected as an initial model for further refinement. The overall resolution of the refined map was estimated using half maps and gold standard FSC (GSFSC) of 0.143. The resolution reported (7.01 Å) was corrected using high-resolution noise substitution to measure the amount of noise overfitting in cryoSPARC (*59*).

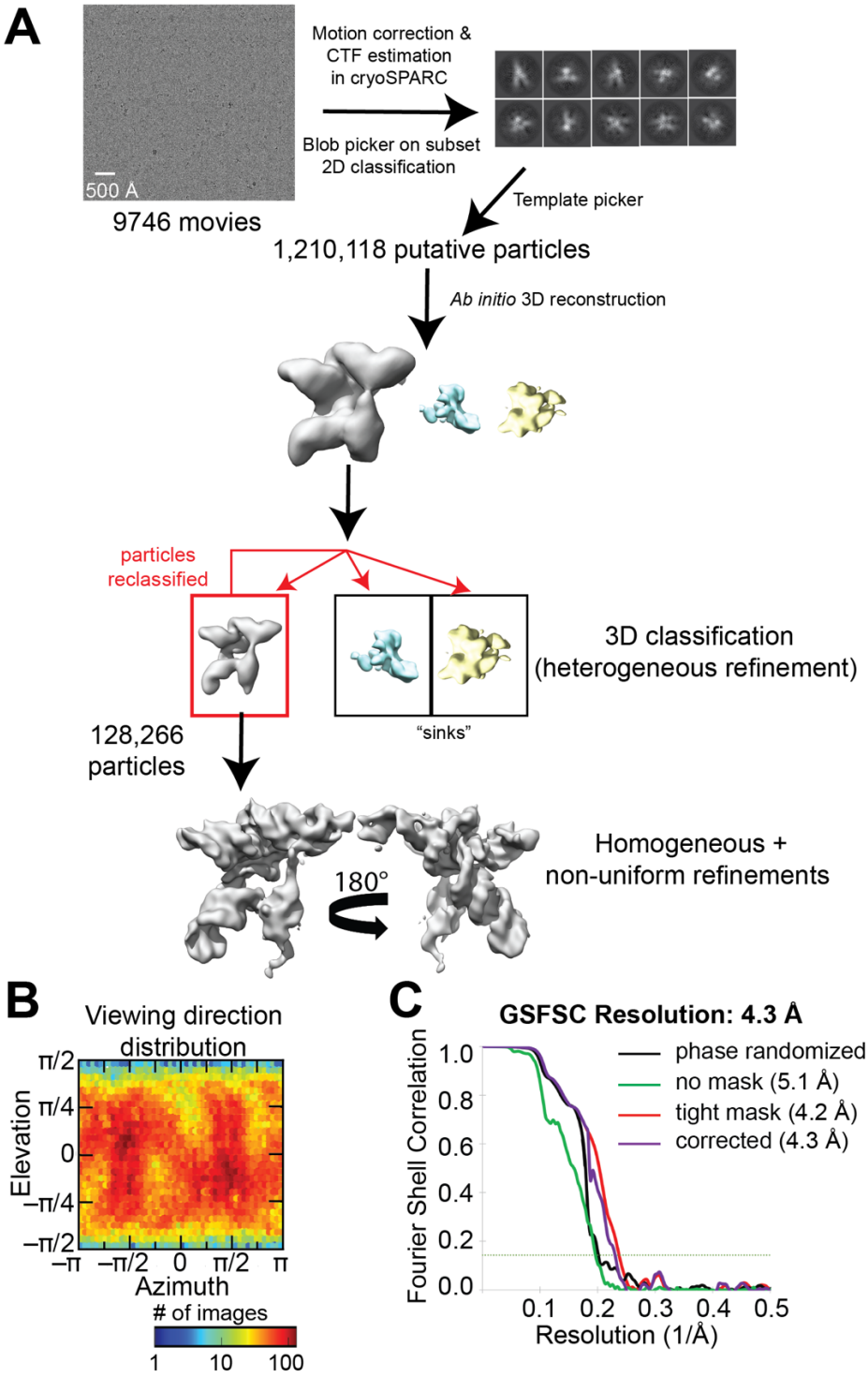

Fig. S3. Analysis of BMV TLS RNA data collected with 300 kV electron microscope. (A) Steps followed to generate cryo-EM reconstruction of BMV TLS using cryoSPARC (*17*). After *ab initio* reconstruction, several rounds of 3D classification (Heterogeneous refinement) were performed to increase the resolution of the map, using bad volumes as 'sinks'. The final map (4.3 Å resolution) was generated using homogeneous refinement followed by a non-uniform refinement with 128,266 particles. (B) Distribution of viewing angles. (C) Estimation of overall resolution of cryo-EM maps using half maps and gold standard FSC of 0.143.

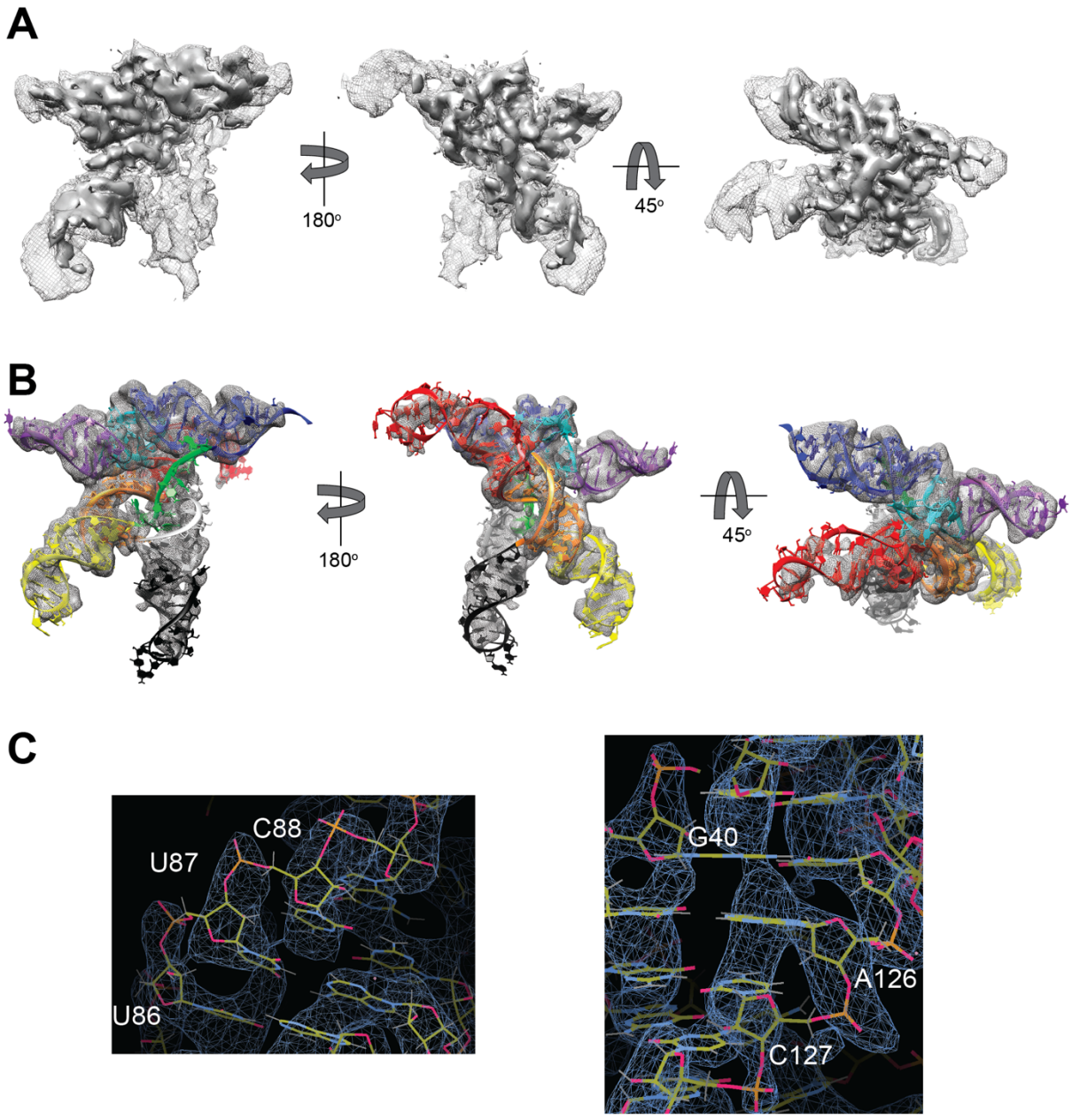

Fig. S4. Model fit to density. (A) 4.3 Å resolution map at two different contour levels to display different features of the map. The map was generated using homogeneous refinement followed by a non-uniform refinement in cryoSPARC with 128,266 particles. The reported resolution was corrected for high-resolution noise overfitting using noise substitution and phase randomized maps (*59*). (B) Structural model of BMV TLS fitted to cryo-EM density. Colors are as in Fig. 2 (C) Examples of density displaying phosphate 'bumps' and base stacking. Map was sharpened using density modification in Phenix (*60*). Figures were generated in Coot (*49*).

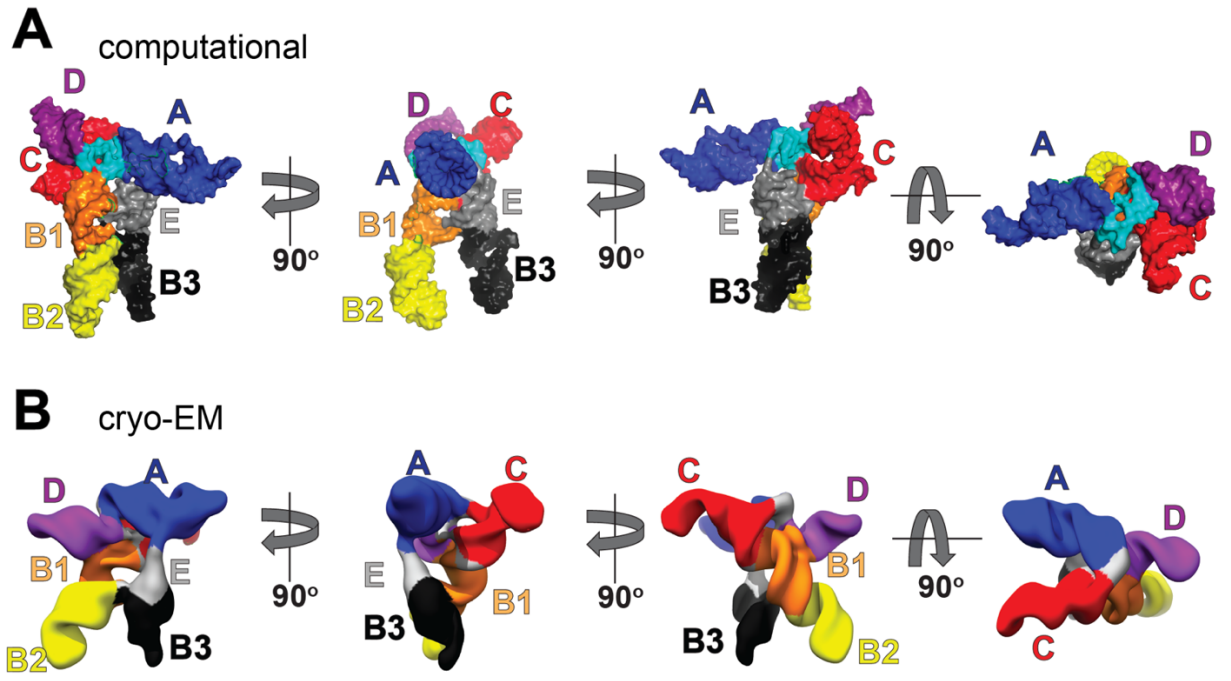

Fig. S5. Comparison between cryo-EM map and published computational model. Helices are colored according to secondary structure in Figure 2A of the main text. (A) Previously published computational model from chemical and enzymatic probing data and phylogenetic secondary structure comparison (*19*). The structure is shown using a solvent-accessible surface representation. (B) The map obtained by cryo-EM is oriented similarly to the computational model in (A) for comparison, with helical elements colored as in panel A. Although global features of the cryo-EM map and the computational model are similar, the location and orientation of the helices differ.

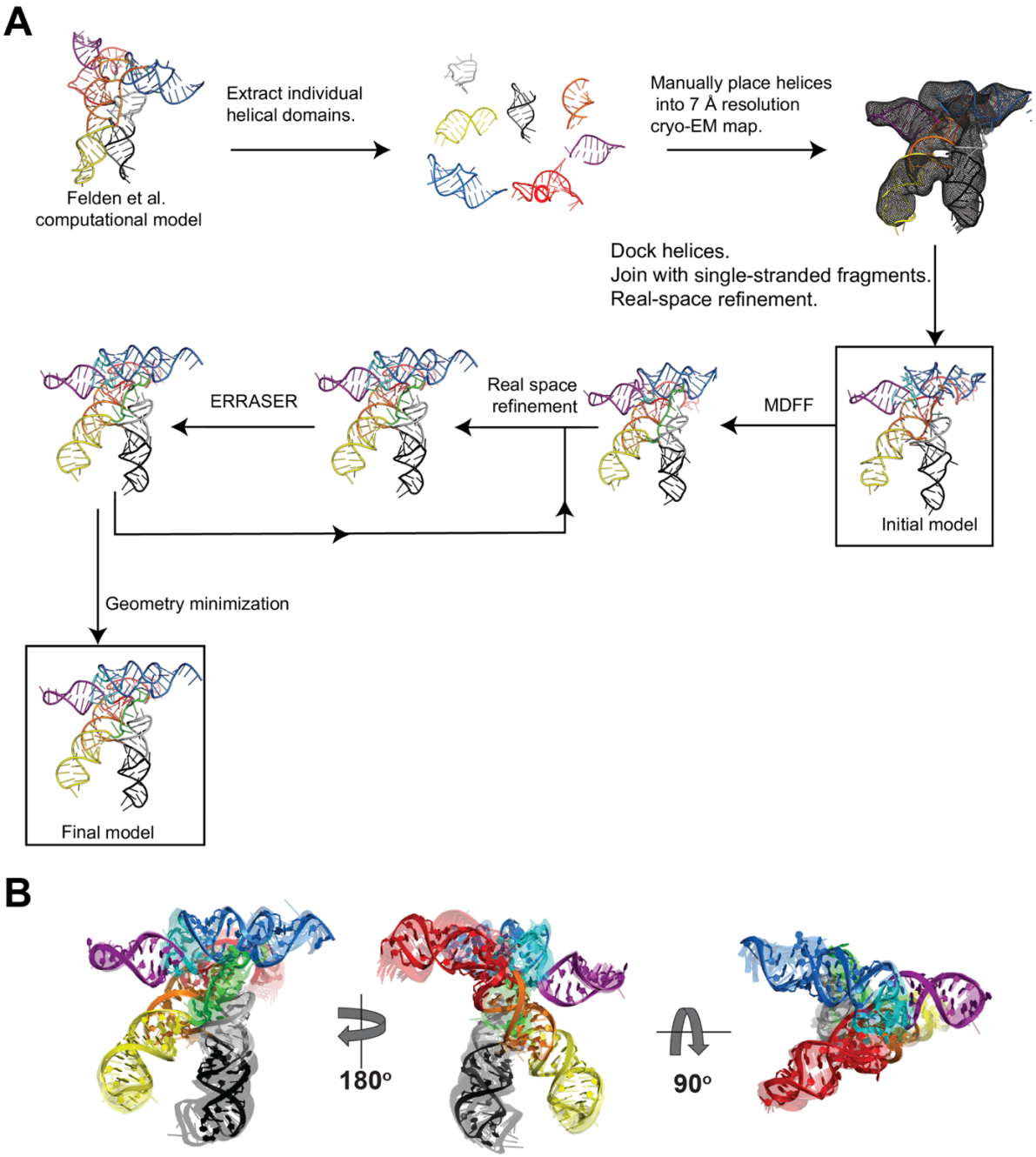

Fig. S6. Structural modelling of BMV TLS. (A) Building a structural model of BMV TLS using manual and automated modelling tools. Details of this process, as well as parameters used, are given in the Materials and Methods section. Briefly, a structural model of BMV TLS was built starting from the computational model of Felden et al., as this model is largely consistent with the experimentally determined secondary structure (*19*). Individual helices were extracted from the computational model and docked into a moderate resolution (~7Å) cryo-EM map using the 'fit in map' function in UCSF Chimera (*47*). Single-stranded regions connecting the helices were added using Chimera and Coot (*49*). A real space refinement (RSR) in Phenix (*51*) was performed to build an initial model of BMV TLS that fit into the low-resolution map. Then we used Namdinator (*50*) to perform molecular dynamics flexible fitting (MDFF; see Material and Methods for critical parameters), using a 4.3 Å map. The model obtained from the MDFF job was then imported back into Phenix for an additional RSR, using the secondary structure of BMV TLS as a constraint. To

correct the geometry of the RNA we used ERRASER (*52, 53*). Several iterations of Phenix RSR and ERRASER were performed to lower the MolProbity clash score and improve the geometry of the model (http://molprobity.biochem.duke.edu) (*54*). A 'Geometry minimization' in Phenix was performed at the end. The final model displayed a MolProbity clashscore of 8.69, 0 bad bonds, 0 bad angles, 28 outlier backbone conformations, and 0 probably wrong sugar puckers (Table S1). (B) Computational modelling of BMV TLS using autoDRRAFTER**.** Ten computational models were generated using autoDRRAFTER (transparent/colored) and are superimposed over the structural model of BMV TLS (opaque/shaded) generated by the method described in (A). autoDRRAFTER is part of the Ribosolve pipeline for accelerated generation of structural models of RNA-only molecules using cryo-EM maps and takes a cryo-EM map, a sequence file, and a secondary structure model as inputs (*22*). The computational models agreed well with our structural model, with RMSD values ranging from 2.0 to 3.2 Å.

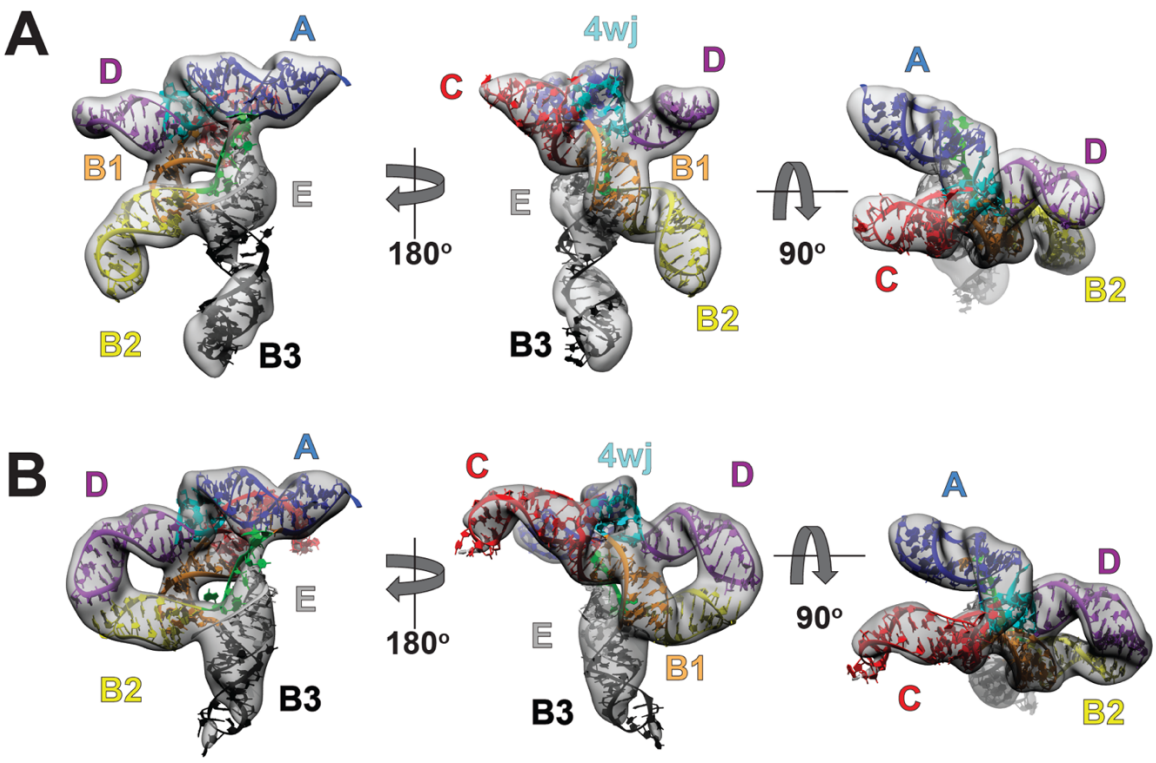

Fig. S7. Structural models of modified constructs support architecture of BMV TLS. (A) Density of $B3^{ext}$+C^{short}, with the structural model docked inside. In this model, extra base pairs have been added to stem B3 and base pairs have been removed from stem C. The density matches a model with these altered helical lengths. (B) Same as panel A, but with D^{ext}+$B2^{short}$. The lengthening of stem D and the shortening of B2 in the model match the density. Unexpectedly, these changes induced a new tertiary contact between the apical loops of B2 and D, apparently due to a fortuitous alignment of the bases in their apical loops.

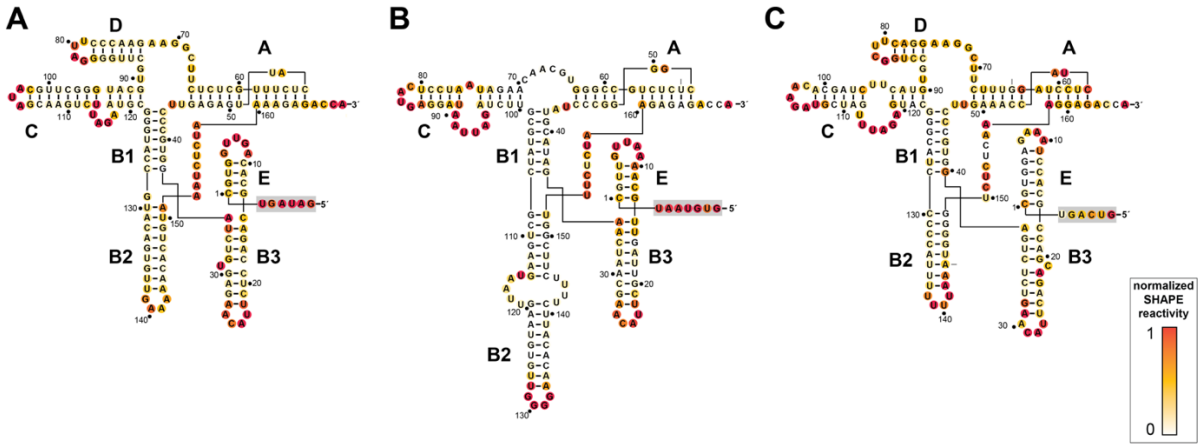

Fig. S8. Chemical probing of representative TLS^{Tyr} variants supports secondary structure consensus model. SHAPE probing of TLS^{Tyr} belonging to three different viruses: (A) BMV, (B) pelargonium zonate spot virus, and (C) cucumber mosaic virus. Helices were labeled using the BMV TLS naming. Structures were drawn to match the consensus sequence and secondary structure model in the main text (Figure 3). Variant from pelargonium zonate spot virus lacks a stem D. 5′ sequences in grey box were added for chemical probing and are not part of the model.

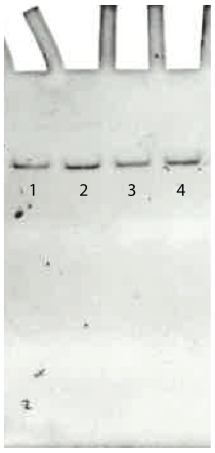

Fig. S9. Gel electrophoresis under native condition of BMV TLS RNA constructs in which specific apical loops were mutated to UUCG. (1) Wild type BMV TLS RNA, (2) E (UUCG), (3) B2 (UUCG), and (4) B3 (UUCG) were folded and run in a 10% polyacrylamide gel with 10 mM $MgCl_2$. The running buffer contained 33 mM TRIS-HCl, 64 mM HEPES, pH 7.4, and 10 mM $MgCl_2$. Electrophoresis was performed in a cold room at 4ºC. RNA was stained with ethidium bromide and imaged with a UV scanner.

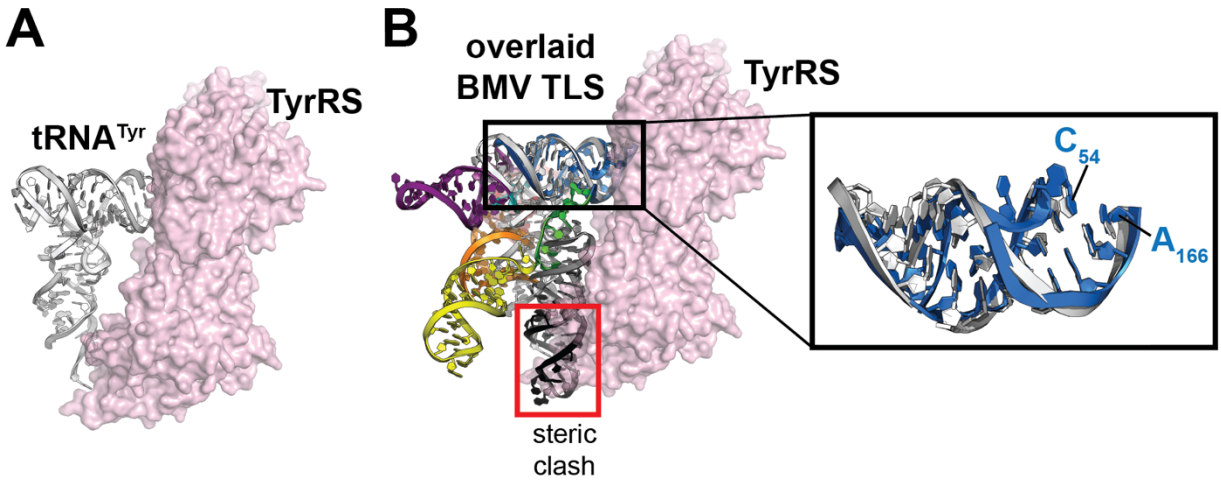

Fig. S10. Modelling of BMV TLS bound to TyrRS suggests that conformational changes are required. (A) Published structure of yeast $tRNA^{Tyr}$ bound to TyrRS homodimer (*25*). Two tRNAs bind to each TyrRS homodimer; for simplicity only one tRNA is shown. (B) Identical structure to panel (A), with BMV TLS superimposed on $tRNA^{Tyr}$ by aligning the structures of the acceptor stems. Boxed: Close-up of the aligned acceptor stems, with tRNA in grey and the BMV TLS stem A in blue. The alignment was performed prioritizing base pairs near the terminal CCA, as this region is known to be critical for tyrosylation (*24*, *25*). Selected nucleotides are labeled for reference.

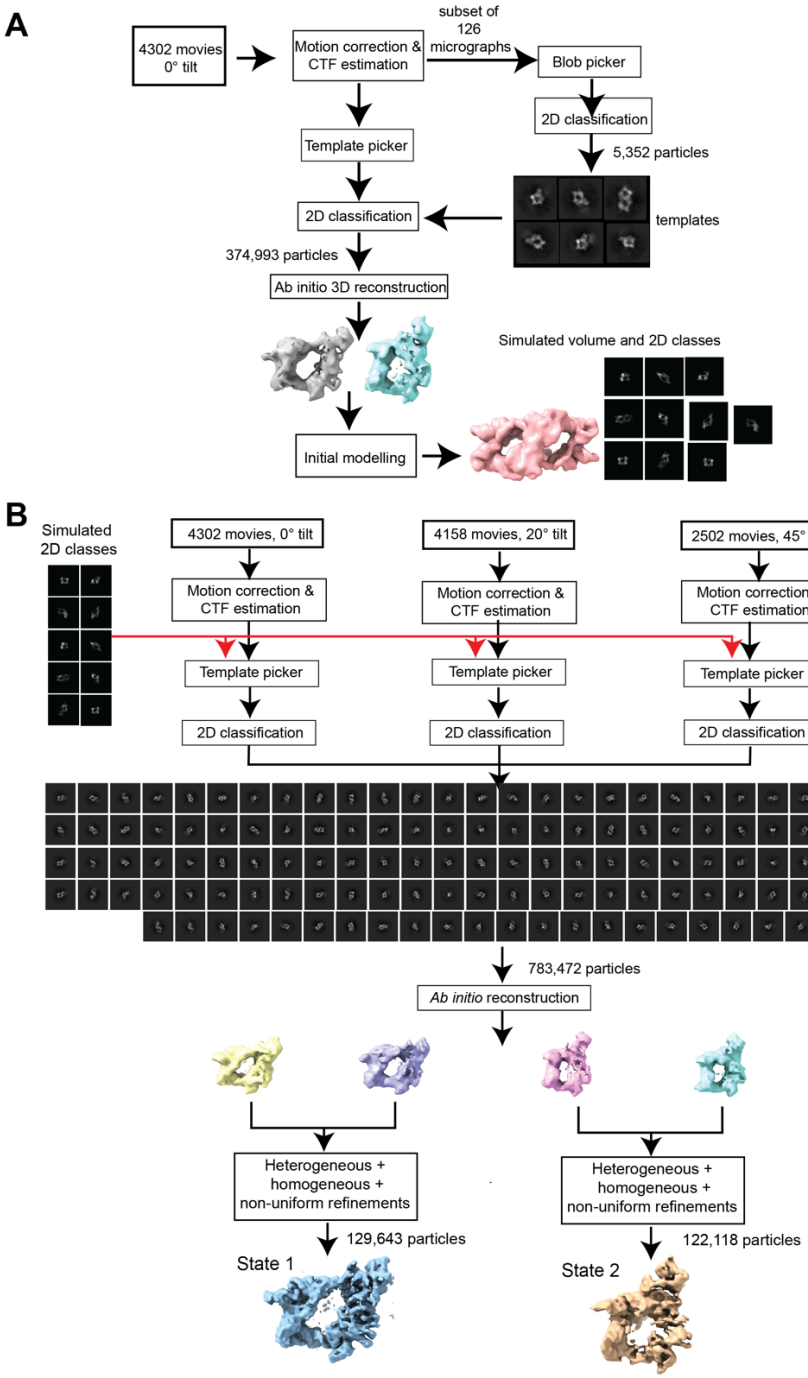

Fig. S11. Analysis of cryo-EM data of the BMV TLS-TyrRS complex. (A) Preliminary analysis of the cryo-EM data collected without tilt. Templates for automated particle picking were generated using blob picker on a subset of 126 micrographs. *Ab initio* reconstructions showed density consistent with BMV TLS RNA bound to TyrRS. These reconstructions were used to generate an initial atomic model of the full complex and a set of simulated 2D projections. (B) Analysis using data collected at three different angles (0º, 20º, and 45º) to reduce preferred orientations. Templates generated in (A) were used to pick particles in all micrographs. The simulated 2D templates were low pass filtered before particle picking, so details of the model do not bias the picking. Two distinct conformations of the bound complex were observed. Although two bound RNAs are seen in multiple 2D classes, one RNA is well-defined in the 3D reconstructions. Bound state 1 was refined to 5.5 Å and bound state 2 to 6.0 Å (Fig. S12).

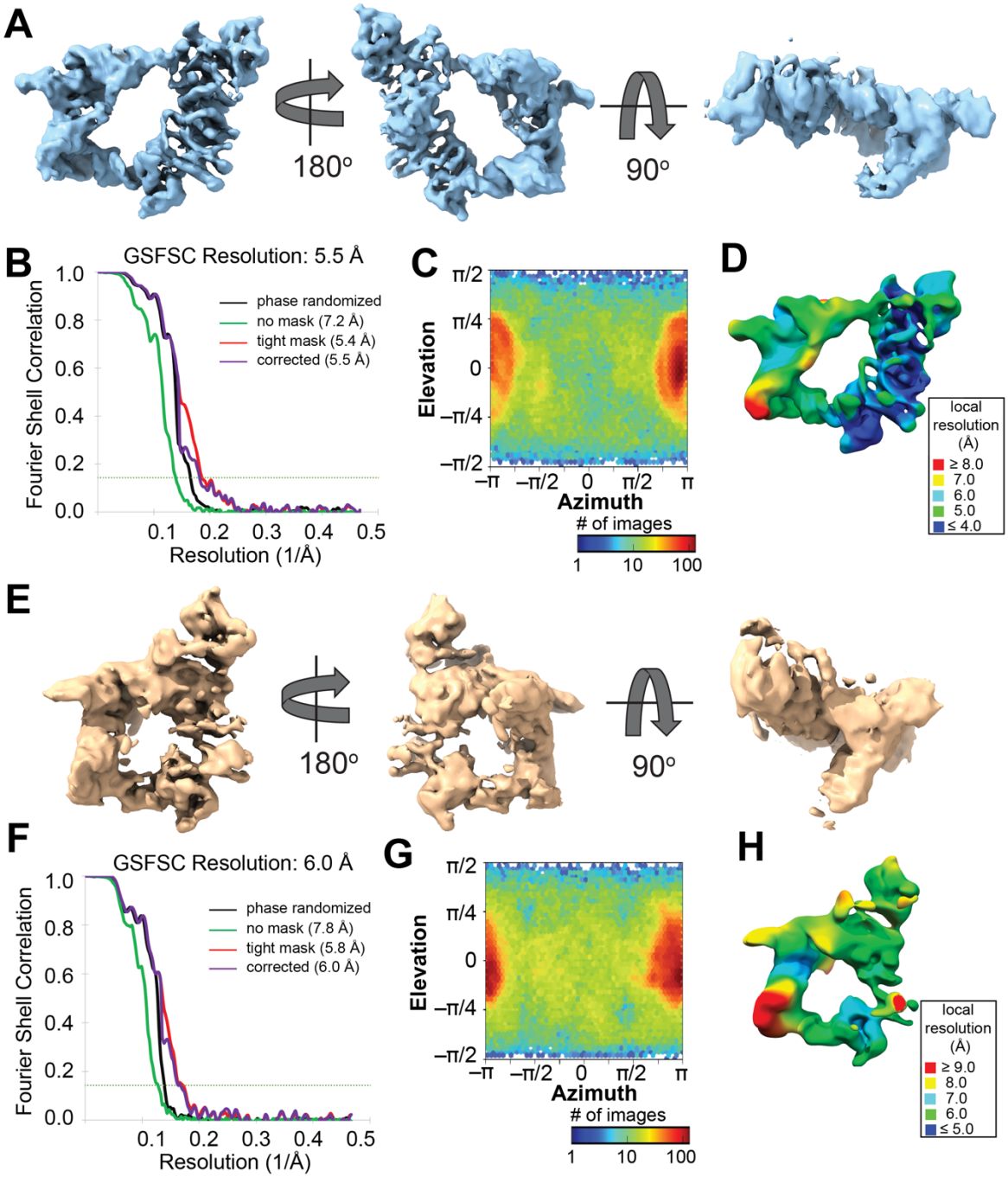

Fig. S12. Refined volumes of two bounds states of the BMV TLS-TyrRS complex. (A) Cryo-EM map of bound state 1, viewed in three different orientations. (B) FSC curves for refined map of bound state 1. Resolutions reported are calculated using gold standard FSC (GSFSC) of 0.143 and were corrected using high-resolution noise substitution to measure the amount of noise overfitting in cryoSPARC (*59*). (C) Distribution of views in the refined map of bound state 1. (D) Local resolution in the cryo-EM map of bound state 1. (E) Cryo-EM map of bound state 2, viewed in three different orientations. (F) FSC curves for refined map of bound state 2. Resolutions reported are calculated using gold standard FSC (GSFSC) of 0.143. (G) Distribution of views in the refined map of bound state 2. (H) Local resolution in the cryo-EM map of bound state 2.

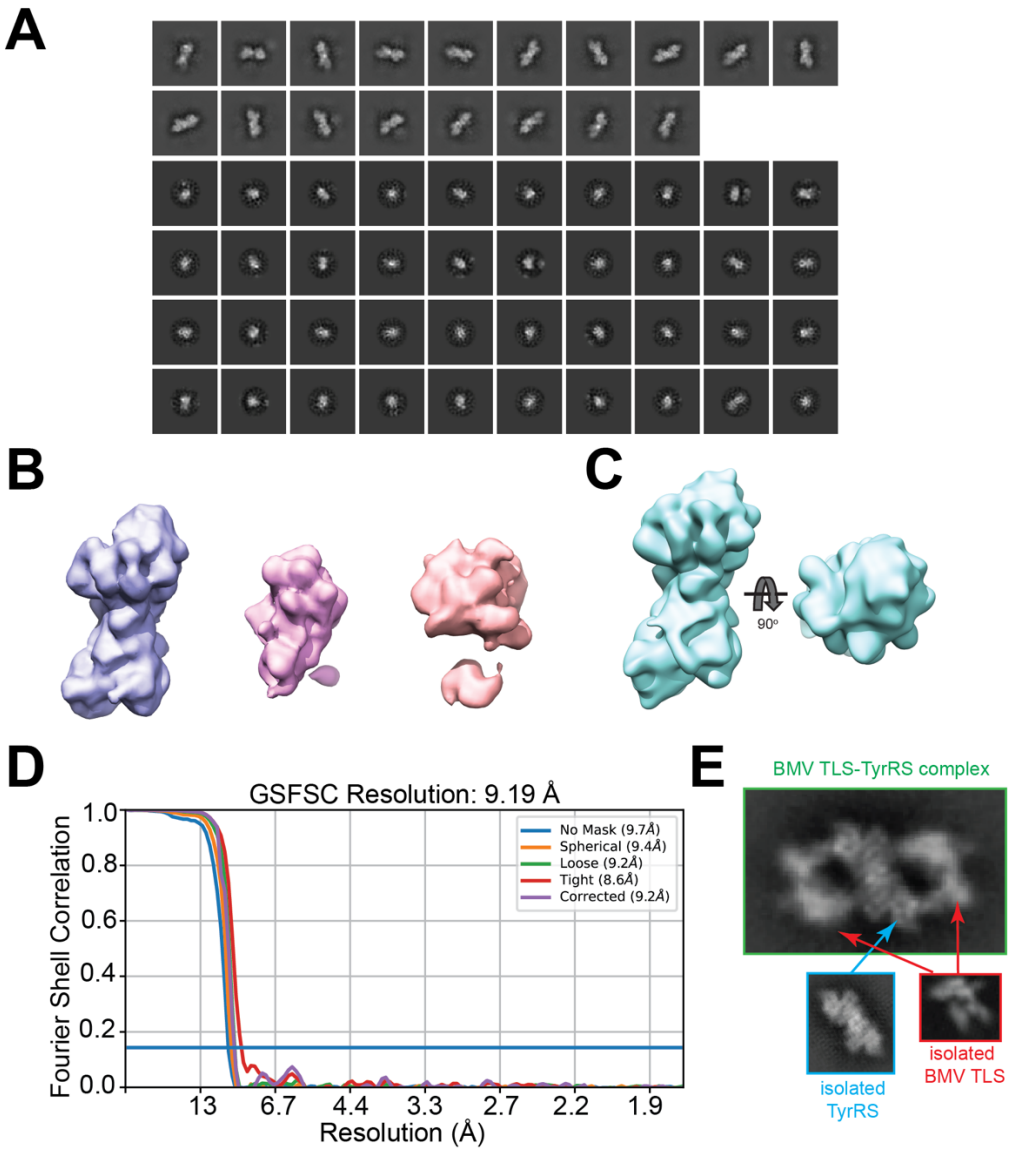

Fig. S13. Cryo-EM studies of purified TyrRS from *Phaseolus vulgaris*. (A) 2D classes of TyrRS after removal of junk particles via 2D classification and selection. Classification showed two major types of classes: side views (long classes; first two rows) and top views (short classes; four bottom rows). Because of the large differences in the dimensions of these two types of classes, they were separated and classified using circular masks of different sizes, as done previously for a protein of similar dimensions (*48*). (B) *Ab initio* 3D reconstructions generated using stochastic gradient descent with cryoSPARC (*17*). The reconstruction on the left (purple volume) agreed with the dimensions expected for TyrRS. (C) Refined volume of TyrRS. (D) Fourier shell correlation (FSC) curves. The overall resolution of the refined map was estimated using half maps and gold standard FSC of 0.143. The resolution reported (9.19 Å) was corrected using high-resolution noise substitution to measure the amount of noise overfitting; the correction utilizes phase randomized maps (*59*). (E) Comparisons of a 2D class of BMV TLS-TyrRS complex (green box), isolated TyrRS (cyan box), and isolated BMV TLS RNA (red box). Density in the middle of the complex corresponds to TyrRS (cyan arrow). Two molecules of BMV TLS RNA can be observed bound to TyrRS (red arrows).

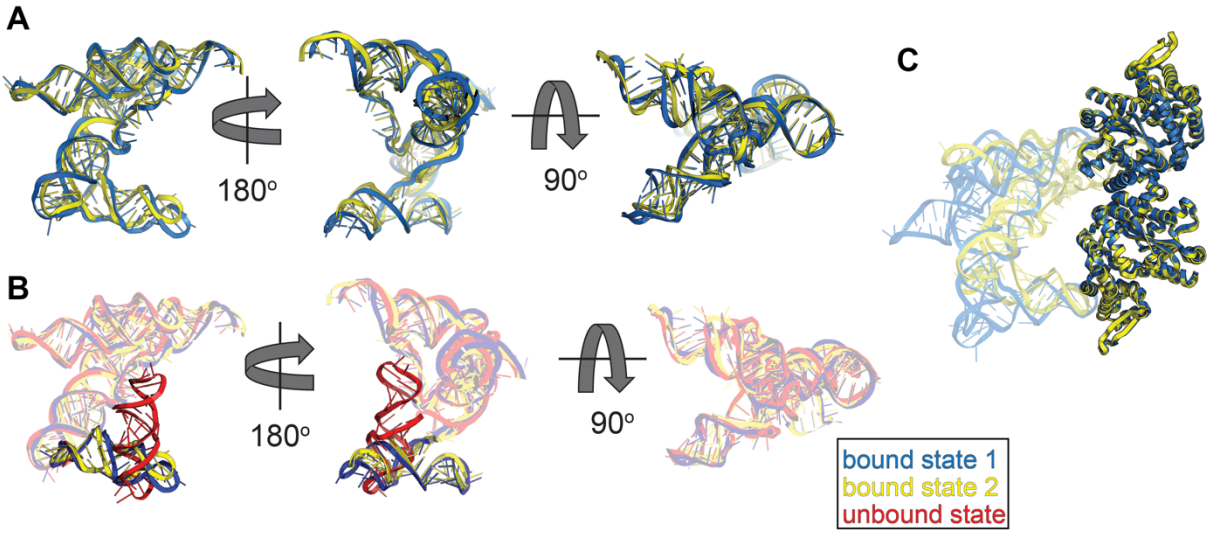

Fig. S14. Comparison between bound and unbound states of BMV TLS RNA. (A) BMV TLS RNA adopts the same global conformation in both bound states. Analysis of the cryo-EM data of BMV TLS-TyrRS complex revealed two different conformational states: bound state 1 (blue) and bound state 2 (yellow). In bound state 1, the acceptor arm of the RNA is not fully docked into the active site (see Fig. 4 in main text). In bound state 2, the acceptor arm is deeper into TyrRS and the 3' CCA is positioned near the active site. Despite these differences, the global conformation of the BMV TLS RNA is essentially the same in both bound states, with an RMSD of 2.78 Å as calculated using the 'align' command in Pymol. (B) Superposition of bound and unbound BMV TLS RNA reveals large conformational changes. In the unbound state (red), B3+E on average occupies a position at roughly a right angle to the acceptor stem analog. In that position B3+E would clash with the TyrRS. In the bound states 1 and 2 (blue and yellow, respectively) B3+E has rotated approximately 90 degrees relative to the unbound conformation and lays roughly parallel to the acceptor stem analog, avoiding any steric clash with the enzyme and placing the B3 apical loop anticodon analog on the surface of TyrRS. (C) The conformation of the TyrRS is essentially the same in both bound states but its position relative to BMV TLS RNA differs. Structures of bound states 1 and 2 are superimposed based on the alignment of TyrRS. The RMSD between the proteins is 0.83 Å as calculated using the 'align' command in Pymol. The bound BMV TLS RNA is transparent.

Table S1. Cryo-EM data collection, refinement, and validation statistics.

	BMV TLS RNA (PDB ID 7SAM, EMDB ID EMD-24952)	TyrRS/BMV TLS Complex, Bound State 1 (PDB ID 7SC6, EMDB ID EMD-25023)	TyrRS/BMV TLS Complex, Bound State 2 (PDB ID 7SCQ, EMDB ID EMD-25041)
Data Collection and Processing			
Microscope	Krios	Krios	Krios
Voltage (KeV)	300	300	300
Camera	Falcon 3 DED	Falcon 3 DED	Falcon 3 DED
Magnification	105,000	105,000	105,000
Pixel size at detector (Å/pixel)	0.413	0.415	0.415
Total electron exposure (e-/Å^2)	30	60	60
No. of frames collected during exposure	28	60	60
Defocus range (μm)	0.8-2.0	0.8-2.5	0.8-2.5
Automation software	SerialEM	SerialEM	SerialEM
Tilt angle (°)	0	0, 20, 45	0, 20, 45
Energy filter slit width (eV)	20	20	20
Micrographs collected (no.)	9,746	10,962	10,962
Total extracted particles (no.)	1,210,118	3,499,339	3,499,339
Reconstruction			
Final refined particles (no.)	128,266	129,643	122,118
Point group	C1	C1	C1
Resolution (Å)	4.3	5.5	6.0
- FSC 0.5 (unmasked/masked)	6.4/5.3	8.8/6.9	9.6/7.5
- FSC 0.143 (unmasked/masked)	5.1/4.3	7.3/5.5	7.9/6.0
Resolution range (local Å)	3.95-11.6	3.8-11.1	X-X
Map sharpening *B* factor (Å^2)	257.7	341.8	398.4
Map sharpening methods	cryoSPARC global sharpening	cryoSPARC global sharpening	cryoSPARC global sharpening
Model Composition			
Protein	0	698	698
RNA	169	169	169
Model Refinement			
Refinement package	Phenix/ERRASER	Phenix	Phenix
- Real or reciprocal space	Real	Real	Real
Model-Map scores			
- CC (box)	0.74	0.74	0.74
- CC (mask)	0.58	0.55	0.50
- CC (volume)	0.57	0.53	0.45
- CC (peaks)	0.50	0.41	0.35
B factors (Å^2) min/max/mean			
- Protein residues	-	162.0/426.7/265.1	277.7/864.1/594.5
- RNA residues	56.74/156.43/103.85	153.4/597.3/328.0	296.1/925.3/576.7
R.m.s deviations from ideal values			
- Bond lengths (Å)	0.001	0.004	0.005
- Bond angles (°)	0.390	0.813	0.945
Model Validation			
MolProbity score	2.23	1.66	2.26
CaBLAM outliers (%)	-	0.72	1.01
Clashscore	2.96	13.11	32.09
Rotamer outliers (%)	-	0.0	0.0
C-beta outliers (%)	-	0.0	0.0
Ramachandran plot			
- Favored (%)	-	97.84	96.11
- Outliers (%)	-	0.0	0.0

Table S2. Sequences of constructs used. Sequence in bold is T7 promoter. Lower case 'gg' was added to facilitate *in vitro* transcription. Sequence in regular font and underlined corresponds to hepatitis delta virus (HDV) ribozyme at the 3' end of desired sequence. Sequence in italic and underlined corresponds to hammerhead (HH) ribozyme at the 5' end of desired sequence. Ribozymes are cleaved as described in Materials and Methods. Sequences in red were added for SHAPE experiments and contain hairpins used for signal normalization. Sequences in parenthesis are UUCG mutations. All sequences were ordered from Integrated DNA Technologies.

Construct	Sequence
BMV TLS gBlock	GCGAGTGAATTC**TAATACGACTCACTATA**ggCGTGGTTG ACACGCAGACCTCTTACAAGAGTGTCTAGGTGCCTTTGAGAGTTACTCT TTGCTCTCTTCGGAAGAACCCTTAGGGGTTCGTGCATGGGCTTGCATAG CAAGTCTTAGAATGCGGGTACCGTACAGTGTTGAAAAACACTGTAAATC TCTAAAAGAGACCA
$B3^{ext}$+C^{short} gBlock	GCGAGTGAATTC**TAATACGACTCACTATA**ggCGTGGTTGACACGCAGAC CTAGTACCTTACAAGGTACTAGTGTCTAGTGCCTTTGAGAGTTACTCTTT GCTCTCTTCGGAAGAACCCTTAGGGGTTCGTGCATGGGCATAGCCTTAG AATGCGGGTACCGTACAGTGTTGAAAAACACTGTAAATCTCTAAAAGAG ACCA
D^{ext}+$B2^{short}$ gBlock	GCGAGTGAATTC**TAATACGACTCACTATA**ggCGTGGTTGACACGCAGAC CTCTTACAAGAGTGTCTAGGTGCCTTTGAGAGTTACTCTTTGCTCTCTTC GGAAGAACAGTTCCTTAGGGAACTGTTCGTGCATGGGCTTGCATAGCAA GTCTTAGAATGCGGGTACCGTACATGAAAATGTAAATCTCTAAAAGAGA CCA
BMV TLS (2'–3' cP) gBlock	GCGAGTGAATTC**TAATACGACTCACTATA**ggCGTGGTTG ACACGCAGACCTCTTACAAGAGTGTCTAGGTGCCTTTGAGAGTTACTCT TTGCTCTCTTCGGAAGAACCCTTAGGGGTTCGTGCATGGGCTTGCATAG CAAGTCTTAGAATGCGGGTACCGTACAGTGTTGAAAAACACTGTAAATC TCTAAAAGAGACCAGGGCGGCATGGTCCCAGCCTCCTCGCTGGCGCCGC CTGGGCAACATGCTTCGGCATGGCGAATGGGACCGGATCCGCGAT
Forward primer for BMV TLS and mutant constructs	AGTGAATTCTAATACGACTCACTATAGG
Reverse primer for BMV TLS and mutant constructs	TGGTCTCTTTTAGAGATTTACAGTG
BMV TLS SHAPE gBlock	GCGAGTGAATTC**TAATACGACTCACTATA**ggAAACGACTCGAGTAGAG TCGAAAAGATAGTCGTGGTTGACACGCAGACCTCTTACAAGAGTGTCTA GGTGCCCTTGAGAGTTACTCTTTGCTCTCTTCGGAAGAACCCTTAGGGGT TCGTGCATGGGCTTGCATAGCAAGTCTTAGAATGCGGGTACCGTACAGT GTTGAAAAACACTGTAAATCTCTAAAAGAGACCAGTTGGAGTCGAGTA GACTCCAACAAAAGAAACAACAACAACAACGGATCCGCGAT
CMV TLS SHAPE gBlock	GCGAGTGAATTC**TAATACGACTCACTATA**ggAAACGACTCGAGTAGAG TCGAAAACGGCTAAAATGGTCAGTCGTGGAGAAATCCACGCCAGCAGA CTTACAAGTCTCTGAGGTGCCCTTGAAACCATCTCCTAGGTTTCTTCGGA AGGACTTCGGTCCGTGTACTTCTAGCACAAGATGCTAGTTTAGAGTACG GGCATCCCCCATTTTTTTAAATGGGGTCTCTCAAAGGAGACCAGTTGGA GTCGAGTAGACTCCAACAAAAGAAACAACAACAACAACGGATCCGCGA T
PZSV TLS SHAPE gBlock	GCGAGTGAATTC**TAATACGACTCACTATA**ggAAACGACTCGAGTAGAG TCGAAAAGTGTAATCGTTGTTAAAACGTTGATTGCTTACAAGCAATCAA GATACGTATCCCGGGGCTCTCTGCCGGGTGCAACAAGATAATCCTCATG AGGATAATTAGATCTTGCGTATCGCTGAAGTAATTGAATGTGTTGGGGA ACACATTCTTTTCTTCGGTTTCTCTAAGAGAGACCAGTTGGAGTCGAGTA GACTCCAACAAAAGAAACAACAACAACAACGGATCCGCGAT
B3_UUCG gBlock	GCGAGTGAATTC**TAATACGACTCACTATA**gg *GT CAAC CACG CTGA TGAG TCCG TGAG GACG AAAC GGTA CCCG GTAC CGTC* CGTGGTTGACACGCAGACCTCT(TTCG)AG AGTG TCTA GGTG CCTT TGAG AGTT ACTC TTTG CTCT CTTC GGAA GAAC CCTT AGGG GTTC GTGC ATGG GCTT GCAT AGCA AGTC TTAG AATG CGGG TACC GTAC AGTG TTGA AAAA CACT GTAA ATCT CTAA AAGA GACC A

B2_UUCG gBlock	GCGAGTGAATTC**TAATACGACTCACTATA**gg *GT CAAC CACG CTGA TGAG TCCG TGAG GACG AAAC GGTA CCCG GTAC CGTC* CGTGGTTGACACG**CAGACCTCTTACAAG AGTG TCT**A GGTG CCTT TGAG AGTT ACTC TTTG CTCT CTTC GGAA GAAC CCTT AGGG GTTC GTGC ATGG GCTT GCAT AGCA AGTC TTAG AATG CGGG TACC GTAC AGTG TT(TTCG)AA CACT GTAA ATCT CTAA AAGA GACC A
E_UUCG gBlock	GCGAGTGAATTC**TAATACGACTCACTATA**gg *TGC GAA CACG CTGA TGAG TCCG TGAG GACG AAAC GGTA CCCG GTAC CGTC* CGTG (TTCG) CA CGCAGACCTCTTACAAG AGTG TCTA GGTG CCTT TGAG AGTT ACTC TTTG CTCT CTTC GGAA GAAC CCTT AGGG GTTC GTGC ATGG GCTT GCAT AGCA AGTC TTAG AATG CGGG TACC GTAC AGTG TTGA AAAA CACT GTAA ATCT CTAA AAGA GACC A
BMV TLS (with 5' HH ribozyme for comparison with UUCG mutants) gBlock	GCGAGTGAATTC**TAATACGACTCACTATA**gg *GT CAAC CACG CTGA TGAG TCCG TGAG GACG AAAC GGTA CCCG GTAC CGTC* CGTGGTTGACACGCAGACCTCTTACAAG AGTG TCTA GGTG CCTT TGAG AGTT ACTC TTTG CTCT CTTC GGAA GAAC CCTT AGGG GTTC GTGC ATGG GCTT GCAT AGCA AGTC TTAG AATG CGGG TACC GTAC AGTG TTGA AAAA CACT GTAA ATCT CTAA AAGA GACC A
Forward primer for SHAPE constructs	GCGAGTGAATTCTAATACGACTCACTATAGG
Reverse primer for SHAPE constructs	GTTGTTGTTGTTGTTTCTTTTGTTGGAGTCTACTC
Fluorescently labeled primer for reverse transcription	5-6FAM/AAAAAAAAAAAAAAAAAAAA TGGTTCCGATGACCCTCGGAAGAGG

References and Notes

1. L. R. Ganser, M. L. Kelly, D. Herschlag, H. M. Al-Hashimi, The roles of structural dynamics in the cellular functions of RNAs. *Nat. Rev. Mol. Cell Biol.* **20**, 474–489 (2019). doi:10.1038/s41580-019-0136-0 Medline

2. Z. A. Jaafar, J. S. Kieft, Viral RNA structure-based strategies to manipulate translation. *Nat. Rev. Microbiol.* **17**, 110–123 (2019). doi:10.1038/s41579-018-0117-x Medline

3. B. M. Akiyama, D. Eiler, J. S. Kieft, Structured RNAs that evade or confound exonucleases: Function follows form. *Curr. Opin. Struct. Biol.* **36**, 40–47 (2016). doi:10.1016/j.sbi.2015.12.006 Medline

4. K. Lu, X. Heng, L. Garyu, S. Monti, E. L. Garcia, S. Kharytonchyk, B. Dorjsuren, G. Kulandaivel, S. Jones, A. Hiremath, S. S. Divakaruni, C. LaCotti, S. Barton, D. Tummillo, A. Hosic, K. Edme, S. Albrecht, A. Telesnitsky, M. F. Summers, NMR detection of structures in the HIV-1 5′-leader RNA that regulate genome packaging. *Science* **334**, 242–245 (2011). doi:10.1126/science.1210460 Medline

5. C. P. Jones, W. A. Cantara, E. D. Olson, K. Musier-Forsyth, Small-angle X-ray scattering-derived structure of the HIV-1 5′ UTR reveals 3D tRNA mimicry. *Proc. Natl. Acad. Sci. U.S.A.* **111**, 3395–3400 (2014). doi:10.1073/pnas.1319658111 Medline

6. D. Yang, J. L. Leibowitz, The structure and functions of coronavirus genomic 3′ and 5′ ends. *Virus Res.* **206**, 120–133 (2015). doi:10.1016/j.virusres.2015.02.025 Medline

7. O. Fernández-Miragall, S. López de Quinto, E. Martínez-Salas, Relevance of RNA structure for the activity of picornavirus IRES elements. *Virus Res.* **139**, 172–182 (2009). doi:10.1016/j.virusres.2008.07.009 Medline

8. X. Shi, S. Bonilla, D. Herschlag, P. Harbury, Quantifying Nucleic Acid Ensembles with X-ray Scattering Interferometry. *Methods Enzymol.* **558**, 75–97 (2015). doi:10.1016/bs.mie.2015.02.001 Medline

9. K. Murata, M. Wolf, Cryo-electron microscopy for structural analysis of dynamic biological macromolecules. *Biochim. Biophys. Acta Gen. Subj.* **1862**, 324–334 (2018). doi:10.1016/j.bbagen.2017.07.020 Medline

10. T. W. Dreher, Viral tRNAs and tRNA-like structures. *WIREs RNA* **1**, 402–414 (2010). doi:10.1002/wrna.42 Medline

11. R. Giegé, Interplay of tRNA-like structures from plant viral RNAs with partners of the translation and replication machineries. *Proc. Natl. Acad. Sci. U.S.A.* **93**, 12078–12081 (1996). doi:10.1073/pnas.93.22.12078 Medline

12. J. A. Hammond, R. P. Rambo, M. E. Filbin, J. S. Kieft, Comparison and functional implications of the 3D architectures of viral tRNA-like structures. *RNA* **15**, 294–307 (2009). doi:10.1261/rna.1360709 Medline

13. T. W. Dreher, Role of tRNA-like structures in controlling plant virus replication. *Virus Res.* **139**, 217–229 (2009). doi:10.1016/j.virusres.2008.06.010 Medline

14. R. L. Joshi, S. Joshi, F. Chapeville, A. L. Haenni, tRNA-like structures of plant viral RNAs: Conformational requirements for adenylation and aminoacylation. *EMBO J.* **2**, 1123–1127 (1983). doi:10.1002/j.1460-2075.1983.tb01556.x Medline

15. M. Vieweger, E. D. Holmstrom, D. J. Nesbitt, Single-Molecule FRET Reveals Three Conformations for the TLS Domain of Brome Mosaic Virus Genome. *Biophys. J.* **109**, 2625–2636 (2015). doi:10.1016/j.bpj.2015.10.006 Medline

16. P. Fechter, R. Giegé, J. Rudinger-Thirion, Specific tyrosylation of the bulky tRNA-like structure of brome mosaic virus RNA relies solely on identity nucleotides present in its amino acid-accepting domain. *J. Mol. Biol.* **309**, 387–399 (2001). doi:10.1006/jmbi.2001.4654 Medline

17. A. Punjani, J. L. Rubinstein, D. J. Fleet, M. A. Brubaker, cryoSPARC: Algorithms for rapid unsupervised cryo-EM structure determination. *Nat. Methods* **14**, 290–296 (2017). doi:10.1038/nmeth.4169 Medline

18. A. Punjani, D. J. Fleet, 3D variability analysis: Resolving continuous flexibility and discrete heterogeneity from single particle cryo-EM. *J. Struct. Biol.* **213**, 107702 (2021). doi:10.1016/j.jsb.2021.107702 Medline

19. B. Felden, C. Florentz, R. Giegé, E. Westhof, Solution structure of the 3′-end of brome mosaic virus genomic RNAs: Conformational mimicry with canonical tRNAs. *J. Mol. Biol.* **235**, 508–531 (1994). doi:10.1006/jmbi.1994.1010 Medline

20. N. J. Baird, S. J. Ludtke, H. Khant, W. Chiu, T. Pan, T. R. Sosnick, Discrete structure of an RNA folding intermediate revealed by cryo-electron microscopy. *J. Am. Chem. Soc.* **132**, 16352–16353 (2010). doi:10.1021/ja107492b Medline

21. T. M. Nakamura, Y. H. Wang, A. J. Zaug, J. D. Griffith, T. R. Cech, Relative orientation of RNA helices in a group 1 ribozyme determined by helix extension electron microscopy. *EMBO J.* **14**, 4849–4859 (1995). doi:10.1002/j.1460-2075.1995.tb00166.x Medline

22. K. Kappel, K. Zhang, Z. Su, A. M. Watkins, W. Kladwang, S. Li, G. Pintilie, V. V. Topkar, R. Rangan, I. N. Zheludev, J. D. Yesselman, W. Chiu, R. Das, Accelerated cryo-EM-guided determination of three-dimensional RNA-only structures. *Nat. Methods* **17**, 699–707 (2020). doi:10.1038/s41592-020-0878-9 Medline

23. V. Perret, C. Florentz, T. Dreher, R. Giege, Structural analogies between the 3′ tRNA-like structure of brome mosaic virus RNA and yeast tRNATyr revealed by protection studies with yeast tyrosyl-tRNA synthetase. *Eur. J. Biochem.* **185**, 331–339 (1989). doi:10.1111/j.1432-1033.1989.tb15120.x Medline

24. P. Fechter, J. Rudinger-Thirion, A. Théobald-Dietrich, R. Giegé, Identity of tRNA for yeast tyrosyl-tRNA synthetase: Tyrosylation is more sensitive to identity nucleotides than to structural features. *Biochemistry* **39**, 1725–1733 (2000). doi:10.1021/bi992276t Medline

25. M. Tsunoda, Y. Kusakabe, N. Tanaka, S. Ohno, M. Nakamura, T. Senda, T. Moriguchi, N. Asai, M. Sekine, T. Yokogawa, K. Nishikawa, K. T. Nakamura, Structural basis for recognition of cognate tRNA by tyrosyl-tRNA synthetase from three kingdoms. *Nucleic Acids Res.* **35**, 4289–4300 (2007). doi:10.1093/nar/gkm417 Medline

26. T. W. Dreher, T. C. Hall, Mutational analysis of the tRNA mimicry of brome mosaic virus RNA: Sequence and structural requirements for aminoacylation and 3′-adenylation. *J. Mol. Biol.* **201**, 41–55 (1988). doi:10.1016/0022-2836(88)90437-8 Medline

27. M. Molinaro, I. Tinoco Jr., Use of ultra stable UNCG tetraloop hairpins to fold RNA structures: Thermodynamic and spectroscopic applications. *Nucleic Acids Res.* **23**, 3056–3063 (1995). doi:10.1093/nar/23.15.3056 Medline

28. W. H. Ward, A. R. Fersht, Asymmetry of tyrosyl-tRNA synthetase in solution. *Biochemistry* **27**, 1041–1049 (1988). doi:10.1021/bi00403a029 Medline

29. T. M. Colussi, D. A. Costantino, J. A. Hammond, G. M. Ruehle, J. C. Nix, J. S. Kieft, The structural basis of transfer RNA mimicry and conformational plasticity by a viral RNA. *Nature* **511**, 366–369 (2014). doi:10.1038/nature13378 Medline

30. A. L. Rao, C. Cheng Kao, The brome mosaic virus 3′ untranslated sequence regulates RNA replication, recombination, and virion assembly. *Virus Res.* **206**, 46–52 (2015). doi:10.1016/j.virusres.2015.02.007 Medline

31. M. R. Chapman, C. C. Kao, A minimal RNA promoter for minus-strand RNA synthesis by the brome mosaic virus polymerase complex. *J. Mol. Biol.* **286**, 709–720 (1999). doi:10.1006/jmbi.1998.2503 Medline

32. C.-H. Kim, C. C. Kao, I. Tinoco Jr., RNA motifs that determine specificity between a viral replicase and its promoter. *Nat. Struct. Biol.* **7**, 415–423 (2000). doi:10.1038/75202 Medline

33. R. Quadt, E. M. Jaspars, Purification and characterization of brome mosaic virus RNA-dependent RNA polymerase. *Virology* **178**, 189–194 (1990). doi:10.1016/0042-6822(90)90393-6 Medline

34. L. Salmon, S. Yang, H. M. Al-Hashimi, Advances in the determination of nucleic acid conformational ensembles. *Annu. Rev. Phys. Chem.* **65**, 293–316 (2014). doi:10.1146/annurev-physchem-040412-110059 Medline

35. K. Zhang, S. Li, K. Kappel, G. Pintilie, Z. Su, T.-C. Mou, M. F. Schmid, R. Das, W. Chiu, Cryo-EM structure of a 40 kDa SAM-IV riboswitch RNA at 3.7 Å resolution. *Nat. Commun.* **10**, 5511 (2019). doi:10.1038/s41467-019-13494-7

36. E. W. Hartwick, D. A. Costantino, A. MacFadden, J. C. Nix, S. Tian, R. Das, J. S. Kieft, Ribosome-induced RNA conformational changes in a viral 3′-UTR sense and regulate translation levels. *Nat. Commun.* **9**, 5074 (2018). doi:10.1038/s41467-018-07542-x Medline

37. I. Kalvari, E. P. Nawrocki, J. Argasinska, N. Quinones-Olvera, R. D. Finn, A. Bateman, A. I. Petrov, Non-Coding RNA Analysis Using the Rfam Database. *Curr. Protoc. Bioinformatics* **62**, e51 (2018). doi:10.1002/cpbi.51 Medline

38. I. Kalvari, J. Argasinska, N. Quinones-Olvera, E. P. Nawrocki, E. Rivas, S. R. Eddy, A. Bateman, R. D. Finn, A. I. Petrov, Rfam 13.0: Shifting to a genome-centric resource for non-coding RNA families. *Nucleic Acids Res.* **46**, D335–D342 (2018). doi:10.1093/nar/gkx1038 Medline

39. R. J. Kohl, T. C. Hall, Aminoacylation of RNA from several viruses: Amino acid specificity and differential activity of plant, yeast and bacterial synthetases. *J. Gen. Virol.* **25**, 257–261 (1974). doi:10.1099/0022-1317-25-2-257 Medline

40. E. P. Nawrocki, S. R. Eddy, Infernal 1.1: 100-fold faster RNA homology searches. *Bioinformatics* **29**, 2933–2935 (2013). doi:10.1093/bioinformatics/btt509 Medline

41. E. Rivas, J. Clements, S. R. Eddy, Estimating the power of sequence covariation for detecting conserved RNA structure. *Bioinformatics* **36**, 3072–3076 (2020). doi:10.1093/bioinformatics/btaa080 Medline

42. P. Cordero, W. Kladwang, C. C. VanLang, R. Das, The mutate-and-map protocol for inferring base pairs in structured RNA. *Methods Mol. Biol.* **1086**, 53–77 (2014). doi:10.1007/978-1-62703-667-2_4 Medline

43. S. Yoon, J. Kim, J. Hum, H. Kim, S. Park, W. Kladwang, R. Das, HiTRACE: High-throughput robust analysis for capillary electrophoresis. *Bioinformatics* **27**, 1798–1805 (2011). doi:10.1093/bioinformatics/btr277 Medline

44. W. Kladwang, T. H. Mann, A. Becka, S. Tian, H. Kim, S. Yoon, R. Das, Standardization of RNA chemical mapping experiments. *Biochemistry* **53**, 3063–3065 (2014). doi:10.1021/bi5003426 Medline

45. H. Kim, P. Cordero, R. Das, S. Yoon, HiTRACE-Web: An online tool for robust analysis of high-throughput capillary electrophoresis. *Nucleic Acids Res.* **41**, W492–W498 (2013). doi:10.1093/nar/gkt501 Medline

46. S. H. Scheres, RELION: Implementation of a Bayesian approach to cryo-EM structure determination. *J. Struct. Biol.* **180**, 519–530 (2012). doi:10.1016/j.jsb.2012.09.006 Medline

47. E. F. Pettersen, T. D. Goddard, C. C. Huang, G. S. Couch, D. M. Greenblatt, E. C. Meng, T. E. Ferrin, UCSF Chimera—A visualization system for exploratory research and analysis. *J. Comput. Chem.* **25**, 1605–1612 (2004). doi:10.1002/jcc.20084 Medline

48. M. A. Herzik Jr., M. Wu, G. C. Lander, High-resolution structure determination of sub-100 kDa complexes using conventional cryo-EM. *Nat. Commun.* **10**, 1032 (2019). doi:10.1038/s41467-019-08991-8 Medline

49. P. Emsley, K. Cowtan, Coot: Model-building tools for molecular graphics. *Acta Cryst.* **D60**, 2126–2132 (2004). doi:10.1107/S0907444904019158 Medline

50. R. T. Kidmose, J. Juhl, P. Nissen, T. Boesen, J. L. Karlsen, B. P. Pedersen, *Namdinator* – automatic molecular dynamics flexible fitting of structural models into cryo-EM and crystallography experimental maps. *IUCrJ* **6**, 526–531 (2019). doi:10.1107/S2052252519007619 Medline

51. D. Liebschner, P. V. Afonine, M. L. Baker, G. Bunkóczi, V. B. Chen, T. I. Croll, B. Hintze, L.-W. Hung, S. Jain, A. J. McCoy, N. W. Moriarty, R. D. Oeffner, B. K. Poon, M. G. Prisant, R. J. Read, J. S. Richardson, D. C. Richardson, M. D. Sammito, O. V. Sobolev, D. H. Stockwell, T. C. Terwilliger, A. G. Urzhumtsev, L. L. Videau, C. J. Williams, P. D. Adams, Macromolecular structure determination using X-rays, neutrons and electrons:

Recent developments in Phenix. *Acta Cryst.* **D75**, 861–877 (2019). doi:10.1107/S2059798319011471 Medline

52. F. C. Chou, P. Sripakdeevong, S. M. Dibrov, T. Hermann, R. Das, Correcting pervasive errors in RNA crystallography through enumerative structure prediction. *Nat. Methods* **10**, 74–76 (2013). doi:10.1038/nmeth.2262 Medline

53. F. C. Chou, N. Echols, T. C. Terwilliger, R. Das, RNA Structure Refinement Using the ERRASER-Phenix Pipeline. *Methods Mol. Biol.* **1320**, 269–282 (2016). doi:10.1007/978-1-4939-2763-0_17 Medline

54. C. J. Williams, J. J. Headd, N. W. Moriarty, M. G. Prisant, L. L. Videau, L. N. Deis, V. Verma, D. A. Keedy, B. J. Hintze, V. B. Chen, S. Jain, S. M. Lewis, W. B. Arendall 3rd, J. Snoeyink, P. D. Adams, S. C. Lovell, J. S. Richardson, D. C. Richardson, MolProbity: More and better reference data for improved all-atom structure validation. *Protein Sci.* **27**, 293–315 (2018). doi:10.1002/pro.3330 Medline

55. J. Jumper, R. Evans, A. Pritzel, T. Green, M. Figurnov, O. Ronneberger, K. Tunyasuvunakool, R. Bates, A. Žídek, A. Potapenko, A. Bridgland, C. Meyer, S. A. A. Kohl, A. J. Ballard, A. Cowie, B. Romera-Paredes, S. Nikolov, R. Jain, J. Adler, T. Back, S. Petersen, D. Reiman, E. Clancy, M. Zielinski, M. Steinegger, M. Pacholska, T. Berghammer, S. Bodenstein, D. Silver, O. Vinyals, A. W. Senior, K. Kavukcuoglu, P. Kohli, D. Hassabis, Highly accurate protein structure prediction with AlphaFold. *Nature* **596**, 583–589 (2021). doi:10.1038/s41586-021-03819-2 Medline

56. E. F. Pettersen, T. D. Goddard, C. C. Huang, E. C. Meng, G. S. Couch, T. I. Croll, J. H. Morris, T. E. Ferrin, UCSF ChimeraX: Structure visualization for researchers, educators, and developers. *Protein Sci.* **30**, 70–82 (2021). doi:10.1002/pro.3943 Medline

57. B. Webb, A. Sali, Comparative protein structure modeling using MODELLER. *Curr. Protoc. Bioinform.* **54**, 5.6.1– 5.6.37 (2016). doi:10.1002/cpbi.3 Medline

58. A. Roy, A. Kucukural, Y. Zhang, I-TASSER: A unified platform for automated protein structure and function prediction. *Nat. Protoc.* **5**, 725–738 (2010). doi:10.1038/nprot.2010.5 Medline

59. S. Chen, G. McMullan, A. R. Faruqi, G. N. Murshudov, J. M. Short, S. H. W. Scheres, R. Henderson, High-resolution noise substitution to measure overfitting and validate resolution in 3D structure determination by single particle electron cryomicroscopy. *Ultramicroscopy* **135**, 24–35 (2013). doi:10.1016/j.ultramic.2013.06.004 Medline

60. T. C. Terwilliger, S. J. Ludtke, R. J. Read, P. D. Adams, P. V. Afonine, Improvement of cryo-EM maps by density modification. *Nat. Methods* **17**, 923–927 (2020). doi:10.1038/s41592-020-0914-9 Medline